JAMES | Journal of Advances in Modeling Earth Systems

RESEARCH ARTICLE
10.1029/2022MS003276

Ocean Barotropic Vorticity Balances: Theory and Application to Numerical Models

Robin Waldman[1] **and Hervé Giordani**[1]

[1]Centre National de Recherches Météorologiques, UMR 3589, Météo France—CNRS, Toulouse, France

Key Points:

- The large-scale ocean circulation includes four distinct vorticity balances for the depth-integrated flow
- Those vorticity balances are discretized in the VoBiN diagnostic module designed for C-grid ocean models such as the NEMO platform
- The barotropic vorticity equation of a global NEMO climate simulation is dominated by Sverdrup and topographic balances

Supporting Information:

Supporting Information may be found in the online version of this article.

Correspondence to:

R. Waldman,
robin.waldman@meteo.fr

Citation:

Waldman, R., & Giordani, H. (2023). Ocean barotropic vorticity balances: Theory and application to numerical models. *Journal of Advances in Modeling Earth Systems*, *15*, e2022MS003276. https://doi.org/10.1029/2022MS003276

Received 29 JUN 2022
Accepted 16 MAR 2023

Abstract The barotropic vorticity (BV) balance is fundamental when interpreting the ocean gyre circulation. Here we propose an intercomparison of vorticity equations for the depth-integrated flow applied to ocean models. We review four distinct variants of the BV balances, each giving access to diagnostic equations for the depth-integrated ocean circulation, either meridional, across geostrophic contours or its divergence. We then formulate those balances in the Vorticity Balances in NEMO (VoBiN) diagnostic package aimed at the NEMO ocean platform and more generally C-grid ocean models. We show that spatial discretization of the equations of motion have profound implications for those vorticity balances. Finally, we diagnose the main balances of a global ocean climate simulation. In all vorticity balances, topographic torques arise from interactions of the flow with slanting topography. We identify significant spurious topographic torques related to the model's C-grid discretizations, and we suggest ways to address them. In the depth-integrated and BV balances, bottom vortex stretching and bottom pressure torque drive the flow interaction with topography, respectively. Contrary to Sverdrup theory, the wind stress curl, although dominant in the interior Subtropics, becomes a minor player anywhere significant bottom velocities prevail. The geostrophic contour vorticity balance highlights the limits of barotropic models of the ocean circulation through the so-called JEBAR term. Finally, the transport divergence vorticity balance stresses the limitations of Ekman plus geostrophic dynamics for the mass balance closure in ocean models. This framework should encourage ocean modellers to diagnose more routinely momentum and vorticity equations.

Plain Language Summary Ocean gyre theories involve the key role played by the wind variations across latitudes to force an interior flow. However, recent work has put forward the role played by bottom topography as a guide, or an obstacle, to the gyre circulation. The general framework employed in those theories is the so-called barotropic vorticity equation involving the balancing of the spin induced by the Earth rotation in an ocean in motion. This work proposes a review on oceanic vorticity balances that synthesizes the informations that they provide about the ocean circulation. We then apply this framework to an ocean model used for climate projections. Our analysis confirms the key role played by interactions with topography in driving the gyre circulation. The ocean bottom topography is a geological constant, so that it constitutes a long-lasting constraint for the circulation. Finally, we also stress the large effect of the ocean circulation formulation in the computer programs that make up an ocean model and should be designed carefully.

1. Introduction

The ocean is a highly turbulent fluid with a Reynolds number of planetary flows as high as a hundred billion. Indeed, the viscosity of saline water is so low that it only becomes a leading-order term of the momentum balance at the millimetric scale. Paradoxically, the Earth's rotation exerts such a large constraint on the flow that over scales larger than a few kilometers, it is rigidified and prevented from developing fully three-dimensional turbulence. Peter Rhines has commented that "Study of the effects of planetary rotation has convinced us that the oceans are less than totally fluid" (Rhines, 1986). Such a rigid behavior of large scale ocean circulation can be described by the so-called vertical vorticity balance (e.g., Vallis, 2006). Indeed, the Coriolis force resulting from the Earth's rotation drives an intense circulation about the local vertical axis which must be balanced in a steady state. This circulation is the result of both the variation of the Earth's spin about the local vertical axis with latitude (the so-called beta effect) and the vertical stretching of water masses subject to the Earth rotation (the so-called planetary vortex stretching). The involvement of both meridional and vertical ocean velocities in the torque of the Coriolis force means that the vorticity balance is a diagnostic tool to constrain both the horizontal and vertical flow.

Vorticity dynamics alone, as any balance derived solely from the momentum equations (Newton's second law), are not sufficient to predict the circulation, which involves the coupling between motion and mass. The displacement of seawater modifies the distribution of its mass, which in turn adjusts the pressure force that drives motion. However, vorticity balances impose such a strong constraint on the flow that they have been a central tool for the analysis of gyre circulations, western boundary currents and zonal jets (e.g., Southern Ocean dynamics). This work focuses on the vorticity balances for the depth-integrated circulation in the horizontal plane. Sverdrup proposed the first dynamical interpretation of oceanic gyres (Sverdrup, 1947). It involves the balance between the beta effect caused by meridional flows and the curl (vertical vorticity) of the turbulent momentum stress at the air-sea interface driven by near-surface winds. Later on, Stommel and Munk solve analytically for models of the gyre circulation by adding a simplified expression for the curl of the bottom stress (Stommel, 1948) and of the lateral dissipation (Munk, 1950) to the vorticity balance. These dissipative contributions allow for an intensified return flow at the western boundary of gyres. Munk and Palmén use the conservation of angular momentum to propose that the Antarctic Circumpolar Current is slowed down by bottom pressure anomaly distribution across major topographic obstacles (Munk & Palmén, 1951). This concept was revisited decades later in the barotropic vorticity (BV) framework to show that topographic pressure torques are also a driver of the gyre circulation (Holland, 1973; Hughes & de Cuevas, 2001; Hughes & Killworth, 1995; Sarkisyan and Ivanov, 1971). In particular, those studies demonstrate that dissipative forces are not necessary for the western boundary return flow to occur. The so-called bottom pressure torques highlight the role of topography as a guide (or an obstacle) to the gyre circulation. Lastly, Fofonoff complements those works by investigating the case of an inertial gyre driven by nonlinear momentum advection (the so-called inertial force) (Fofonoff, 1954). He shows from the conservation of absolute vorticity that if inertial forces are comparable in magnitude to the Coriolis force, a free steady gyre-like circulation is allowed. This concept is used decades later to interpret the western intensification of gyres by inertial torques (e.g., Böning, 1986).

Vorticity balances have been extensively used by ocean modellers in idealized settings assuming a barotropic (depth-independent) circulation and/or a flat bottom (Böning, 1986; Bryan & Cox, 1972; LaCasce & Isachsen, 2010; Patmore et al., 2019). By construct, such settings neglect the effect of topography on the horizontal flow and/or its large modulation by baroclinic (depth-dependent) adjustments of the circulation. Studies with a flat bottom and weak inertial forces generally find a reasonable agreement of gyre transports with the Sverdrup theory, which is notorious for providing poor (generally too low, e.g., Thomas et al., 2014) transport estimations outside the interior of subtropical gyres. Studies with variable topography but a barotropic ocean overestimate the topographic constraint on the flow as a consequence of too large bottom velocities and associated bottom pressures. A series of idealized configurations were proposed which addressed the effects of variable topography and baroclinicity on the depth-integrated circulation (Borowski et al., 2002; Hendershott & Rizzoli, 1976; Jackson et al., 2006; Jagannathan et al., 2021; Jouanno & Capet, 2020; Olbers & Eden, 2003; Olbers & Lettmann, 2007; Stewart et al., 2021). In parallel, a limited number of studies have addressed the vorticity of the depth-integrated circulation in three-dimensional numerical simulations with realistic topography and external forcings (Bell, 1999; Ezer & Mellor, 1994; Gula et al., 2015; Hughes & de Cuevas, 2001; Le Bras et al., 2019; Le Corre et al., 2020; Myers et al., 1996; Schoonover et al., 2016; Sonnewald et al., 2019; Spence et al., 2012; Styles et al., 2022; Wang et al., 2017; Yeager, 2015). Overall, these studies highlight the limitations of the Sverdrup balance and the importance of the topographic, baroclinic and inertial torques. They also stress the limitations related to the formulations of lateral and bottom boundary conditions in ocean models.

However, most of the BV analysis in ocean models remains limited to the computation of Sverdrup transports. The main reason for this is practical: Sverdrup transports are trivially deduced from the surface wind stress field, whereas the remaining BV contributions require the online storage of the momentum trend equation, which still remains a rare practice in the ocean modeling community. In addition, this diagnostic tends to be very noisy at the model grid scale and to our knowledge, only Styles et al. (2022) have documented the origins and consequences of such noise. On top of those practical obstacles, the theoretical background is heterogeneous with a diversity of alternative (and not equivalent) formulations for the BV balance. The aim of this work is thus to provide a theoretical framework for the analysis of BV balances in ocean models and to apply it in a global ocean climate model. In Section 2, we show that there exist four distinct vorticity balance formulations for the depth-integrated ocean circulation. In Section 3, we re-formulate those equations in a diagnostic package aimed at the NEMO and mode generally C-grid modeling platforms to show the consequences of model discretizations on the main physical torques. In Section 4, we make use of those discretized equations in a global NEMO ocean climate simulation to

find the dominance of topographic effects, both physical and numerical. We discuss our main results in Section 5 and summarize the main findings in Section 6.

2. Vorticity Balances of the Depth-Integrated Ocean Circulation

2.1. Momentum and Vorticity Balance

As detailed in Appendix A1, the large-scale ocean circulation is driven by the Boussinesq momentum equations which in the local Cartesian coordinate frame are:

$$\frac{\partial \mathbf{u_h}}{\partial t} = \mathbf{A} + \mathbf{D} + \mathbf{F} - f\,\mathbf{k} \times \mathbf{u_h} - \frac{1}{\rho_0}\boldsymbol{\nabla}_\mathbf{h} P \tag{1}$$

$$\frac{\partial P}{\partial z} = -\rho g^* \tag{2}$$

with $\mathbf{u_h}$ the horizontal velocity vector, $\mathbf{A}$ the nonlinear advection, $\mathbf{D}$ the horizontal dissipation, $\mathbf{F}$ the vertical friction trend, f the Coriolis parameter, $\mathbf{k}$ the local vertical unit vector, P the perturbation pressure, ρ the in situ density and g^* the gravity acceleration. Dimensional analysis reveals that away from frictional boundary layers, the leading-order balances for the large-scale circulation are the geostrophic and hydrostatic balances (e.g., Vallis, 2006). Those balances involve the Coriolis, pressure and buoyancy forces and have been extremely useful for oceanographers to estimate currents from the simple knowledge of density, dynamic sea level and/or dynamic pressure. Deviations from the geostrophic balance are second-order because they only account for a small fraction of the total velocity and dynamic pressure fields. However, they can be significant in the vorticity budget and constrain the ocean circulation. They are also necessary to break the steadiness inherent to purely geostrophic flows. This is the initial motivation for formulating the vertical vorticity balance of the ocean circulation.

Cross-differentiating Equation 1 and using continuity yields:

$$\frac{\partial \zeta}{\partial t} = \mathrm{Curl}(\mathbf{A}) + \mathrm{Curl}(\mathbf{D}) + \mathrm{Curl}(\mathbf{F}) - \beta v + f\frac{\partial w}{\partial z} \tag{3}$$

with $\zeta = \frac{\partial v}{\partial x} - \frac{\partial u}{\partial y}$ the relative vertical vorticity, $\mathrm{Curl}(\mathbf{a}) = \frac{\partial a_y}{\partial x} - \frac{\partial a_x}{\partial y}$ the vertical vorticity operator with $\mathbf{a}$ an arbitrary vector, $\beta = \frac{df}{dy}$ and w the vertical velocity. The terms of Equation 3 are the local vorticity trend, the vorticity generated by nonlinear advection, lateral dissipation and vertical friction, the beta effect and the planetary vortex stretching. As shown in Appendix A2, this equation can be recast as a function of relative vortex stretching and tilting, but with the practical challenge of requiring an explicit decomposition of the nonlinear advection term. The local Boussinesq pressure force being a gradient function, it generates no vorticity in the flow. As a consequence, for a geostrophic flow, the meridional and vertical velocities are restricted to the balance between beta effect and planetary vortex stretching. For additional meridional and/or vertical motion to occur, the vorticity generated by the Coriolis force must be balanced by second-order terms of the momentum equations: local vorticity trend and vorticity of nonlinear advection, lateral dissipation and vertical friction. As we will show below, this constraint is even stronger when integrating the vorticity balance over the full depth.

2.2. Depth-Integrated Vorticity Balance

A natural formulation for the depth-integrated vorticity balance is obtained by integrating vertically Equation 3 which yields:

$$<\frac{\partial \zeta}{\partial t}> \simeq < \mathrm{Curl}(\mathbf{A}) > + < \mathrm{Curl}(\mathbf{D}) > + \frac{1}{\rho_0}(\mathrm{Curl}(\tau_\mathbf{s}) - \mathrm{Curl}(\tau)_b) - f w_b - \beta V \tag{4}$$

with $<a> = \int_{-h}^{\eta} a\,dz$ the vertical integral operator of an arbitrary function a from the bottom depth $-h$ (with $h > 0$) to the sea surface η, $V = \int_{-h}^{\eta} v\,dz$ the vertically-integrated meridional transports and

$$\int_{-h}^{\eta} \mathrm{Curl}(\mathbf{F})\,dz = \frac{1}{\rho_0}(\mathrm{Curl}(\tau)_s - \mathrm{Curl}(\tau)_b) \tag{5}$$

Subscripts s and b stand for surface ($z = \eta$) and bottom ($z = -h$), respectively. In Equation 4, we have neglected sea level variations to write $\mathrm{Curl}(\tau)_s \simeq \mathrm{Curl}(\tau_\mathbf{s})$ and the surface vertical velocity $w_s \simeq 0$ given that they are several

Table 1
Summary of the Four Vorticity Balances for the Depth-Integrated Oceanic Circulation

Name	Equation number	Trend	Diagnosed transport	Wind forcing	Topographic torque
Depth-integrated vorticity balance	4	Depth-integrated vorticity	Depth-integrated meridional transport	Wind stress curl	Bottom vortex stretching
Barotropic vorticity balance	10	Barotropic vorticity = vorticity of the depth-integrated flow	Depth-integrated meridional transport	Wind stress curl	Bottom pressure torque
Geostrophic contour vorticity balance	12	Vorticity of the depth-average flow	Depth-integrated transport across geostrophic $\frac{f}{h}$ contours	Curl of wind stress per unit depth	Joint Effect of Baroclinicity and Relief (JEBAR) = baroclinic pressure torque
Transport divergence vorticity balance	16	Vorticity of the depth-integrated flow over f	Depth-integrated transport divergence	Ekman pumping	Geostrophic transport divergence

Note. The topographic torque indicates the terms arising from variable topography, as opposed to bottom friction (all cases) and the nonlinear and dissipative torques per unit depth (Equation 12) which are not specific to variable topography.

orders of magnitude lower than their bottom counterpart. See Appendix A3 for a discussion on surface vertical velocities and the so-called Goldsbrough-Stommel circulation (Huang & Schmitt, 1993). The terms of Equation 4 are the depth-integrated vorticity trend and vorticity of nonlinear advection and lateral dissipation, the surface minus bottom frictional stress curl, the bottom planetary vortex stretching and the (depth-integrated) beta effect.

The first entry of Table 1 summarizes the main properties of this balance. The strong constraint on the horizontal flow and the role of second-order terms appear immediately by considering first a purely geostrophic flow (assuming only planetary beta effect and vortex stretching are non-zero). In this case, meridional transports are permitted if and only if bottom velocities are non-zero, hence requiring variable topography. In the general case, second-order terms of Equation 1 also play a key role in the forcing of meridional motion. On the right-hand side of Equation 4, we find Fofonoff's nonlinear advection, Munk's lateral dissipation, Sverdrup's wind stress curl and Stommel's bottom stress curl balancing the vorticity of the Coriolis force. The vorticity trend term can also absorb some unbalanced vorticity source in the short term, but in the long run (typically yearly integration) it becomes negligible. Dividing Equation 4 by βh yields a depth-average velocity balance, while dividing by f or β yields balance equations for the bottom vertical velocity or meridional transports.

Figure 1a illustrates the depth-integrated vorticity balance in a northern subtropical gyre assuming geostrophic and surface Ekman dynamics. In the interior ocean, the Sverdrup balance between the wind stress curl and the meridional transport is modified by the presence of a topographic obstacle. If bottom velocities are non-zero, the flow must either accelerate or flow around the obstacle in order to maintain its vorticity balance. Along the western boundary, a bottom vertical motion is sufficient to balance the strong beta effect caused by the intensified western return flow. Namely, the bottom vorticity stretching caused by downward motion associated with an offshore transport is able to balance the beta effect.

2.3. Barotropic Momentum Balance

We will now show, following Hughes and Killworth (1995), that there are three additional formulations for the vorticity balance of the depth-integrated ocean circulation. For that, we must formulate the depth-integral of the momentum Equation 1 first. The Coriolis force becomes:

$$-f\mathbf{k}\times\mathbf{U_h} = f\nabla_h\Psi \tag{6}$$

where $\mathbf{U_h} = \int_{-h}^{\eta}\mathbf{u_h}dz$ is the depth-integrated horizontal transport and we have used the depth-integrated continuity $\nabla_h\cdot\mathbf{U_h}\simeq 0$ (assuming again that $w_s\simeq 0$) to introduce the barotropic stream function Ψ such that $\frac{\partial\Psi}{\partial x} = V$ and $\frac{\partial\Psi}{\partial y} = -U$. We use the hydrostatic relation (Equation 2) to express the dynamic pressure as a bottom plus hydrostatic (baroclinic) component:

$$P(z) = P_b - g^*\int_{-h}^{z}\rho dz' \tag{7}$$

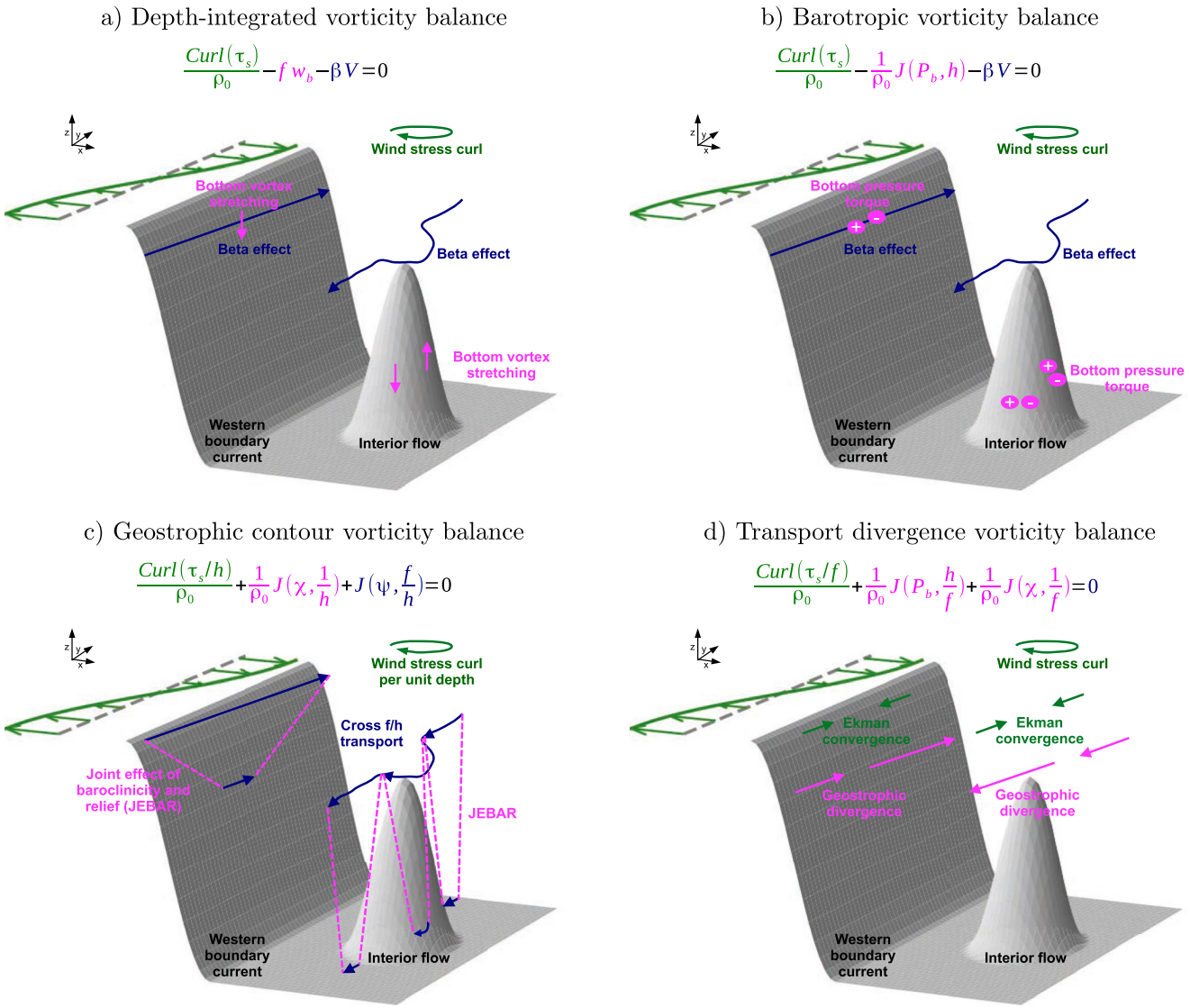

Figure 1. Schematic of the four depth-integrated oceanic vorticity balances in a northern subtropical gyre with a western boundary slope and an interior obstacle, assuming geostrophic and surface Ekman dynamics. Wind-driven torques are in green, topographic torques in magenta and transport-driven torques in blue. Panels (a, b) highlight the balancing of the flow by topographic interactions. Panel (c) stresses the mitigation of this topographic effect by the flow weakening at depth. Panel (d) expresses the mass conservation as a balancing of Ekman convergence and geostrophic divergence.

We deduce the depth-integrated pressure force as:

$$-\frac{1}{\rho_0} < \nabla_h P > = -\frac{1}{\rho_0}(h\nabla_h P_b + \nabla_h \chi) \tag{8}$$

where we have used the Leibniz integration formula and the double integration rule, and neglected sea surface height given $\eta \ll h$. $\chi = g^* \int_{-h}^{0} \rho z dz$ is the baroclinic potential energy. Its horizontal gradient drives depth-integrated baroclinic geostropic transports. It has been extensively used in the context of Southern Ocean dynamics (Böning et al., 2008; Borowski et al., 2002; Hughes & Killworth, 1995; Olbers et al., 2004; Saenko et al., 2005) but has been largely overlooked by oceanographers outside of this region (Waldman et al., 2020). Finally, depth integration of Equation 1 yields:

$$\frac{\partial \mathbf{U_h}}{\partial t} = < \mathbf{A} > + < \mathbf{D} > + \frac{1}{\rho_0}(\tau_s - \tau_b) + f\nabla_h \Psi - \frac{1}{\rho_0}(h\nabla_h P_b + \nabla_h \chi) \tag{9}$$

where consistently with Equation 8 we have neglected sea surface height.

In Appendix A4, we discuss the characteristics of this equation and the consequence for the analysis of ocean circulation along them. More relevant to this work, we can construct three distinct vorticity balances from Equation 9, each eliminating one out of three geostrophic terms (the last three terms of Equation 9) and providing dynamical constraints on the remaining two. Equation 9 is a depth-integrated force balance. The baroclinic pressure force exerts no depth-integrated torque because it is the gradient function of χ. Equation 9/h is a depth-average force balance. The bottom pressure force exerts no depth-averaged torque because it is the gradient function of P_b. Equation 9/*f* is a depth-integrated transport equation: it expresses the balancing of the Coriolis force in terms of depth-integrated transports. This latter exerts no torque because it is the gradient function of Ψ, that is, because depth-integrated transports are to a good approximation non-divergent. We develop below those three additional vorticity balances for the depth-integrated flow.

2.4. Barotropic Vorticity Balance

The second depth-integrated vorticity balance is referred to as the so-called barotropic vorticity (BV) balance. It is obtained by taking the curl of Equation 9, yielding:

$$\frac{\partial Z}{\partial t} = \mathrm{Curl}(<\mathbf{A}>) + \mathrm{Curl}(<\mathbf{D}>) + \frac{1}{\rho_0}\mathrm{Curl}(\tau_\mathbf{s} - \tau_\mathbf{b}) - \beta V + \frac{1}{\rho_0} J(P_b, h) \tag{10}$$

where $Z = \mathrm{Curl}\ (\mathbf{U_h})$ is the BV and $J(a,b) = \frac{\partial a}{\partial x}\frac{\partial b}{\partial y} - \frac{\partial a}{\partial y}\frac{\partial b}{\partial x}$ the Jacobian operator, with a and b two arbitrary scalars. Again, we have neglected horizontal variations of the free surface, given that $\eta \ll h$, so that the sea level contribution to the bottom pressure torque $\frac{1}{\rho_0} J(P_b, \eta)$ can be neglected. Equation 10 has been by far the most widespread BV balance in the ocean modeling community (e.g., Le Corre et al. (2020) and references therein). A practical convenience of Equation 10 is that contrary to Equation 4, no decomposition is required for the Coriolis term which only includes the beta effect as a consequence of the depth-integrated continuity. The topographic influence on the flow is separately diagnosed from the bottom pressure torque (last term of Equation 10) which quantifies the vorticity of the pressure force exerted by solid Earth onto the fluid.

The second entry of Table 1 summarizes the main properties of this balance. Equations 4 and 10 are very similar but they should be viewed as siblings rather than twins. There have been attempts by modellers to identify the bottom stretching of Equation 4 with the bottom pressure torque of Equation 10 (Bell, 1999; Spence et al., 2012; Wang et al., 2017). However, bottom velocities are next to boundaries and should not be assumed geostrophic, as shown by Le Corre et al. (2020). Indeed, substracting Equation 10 from Equation 4 gives a formulation for the difference between bottom stretching and bottom pressure torque as the sum of bottom ageostrophic torques (or equivalently vertical velocities):

$$-f w_b - \frac{1}{\rho_0} J(P_b, h) = \mathbf{k} \times \left[\mathbf{A} + \mathbf{D} + \mathbf{F} - \frac{\partial \mathbf{u_h}}{\partial t}\right]_b \cdot \nabla_h h \tag{11}$$

where we have used the Leibniz integration formula. Therefore, the bottom torque of the nonlinear advection, dissipation, frictional and trend terms of Equation 1 are sources of bottom vertical velocities and they explain the difference between bottom stretching and bottom pressure torque. In a recent idealized study, Jagannathan et al. (2021) showed that the frictional contribution to Equation 11, called the bottom stress divergence torque, is the dominant contribution to the bottom pressure torque in models that resolve the bottom boundary layer, hence highlighting the differences between bottom pressure torque and bottom vortex stretching. Nevertheless, the physical interpretation of Equations 4 and 10 is similar, and both of these latter terms represent the flow interaction with topography. In particular, Equation 10 can also be divided by β or βh to obtain a meridional transport or a depth-average meridional velocity balance equation.

We illustrate again this balance in a northern subtropical gyre assuming geostrophic and surface Ekman dynamics (Figure 1b). In the interior ocean, the Sverdrup balance between the wind stress curl and the meridional transport is modified by the presence of a topographic obstacle. If bottom geostrophic velocities are non-zero, or equivalently if bottom pressure varies along isobaths, the flow must either accelerate or flow around the obstacle in order to maintain its vorticity balance. Along the western boundary, the same bottom pressure torque is sufficient to balance the strong beta effect caused by the intensified western return flow. Namely, the bottom pressure increase along isobaths deviates the flow toward deeper isobaths and is able to balance the beta effect.

2.5. Geostrophic Contour Vorticity Balance

The third depth-integrated vorticity balance is obtained by taking the curl of Equation 9 divided by h, yielding:

$$\mathrm{Curl}\left(\frac{\partial \mathbf{U_h}/h}{\partial t}\right) = \mathrm{Curl}\frac{<\mathbf{A}>}{h} + \mathrm{Curl}\frac{<\mathbf{D}>}{h} + \frac{1}{\rho_0}\mathrm{Curl}\left(\frac{\tau_s - \tau_b}{h}\right) + J\left(\Psi, \frac{f}{h}\right) + \frac{1}{\rho_0}J\left(\chi, \frac{1}{h}\right) \quad (12)$$

The last two terms are respectively the transport across geostrophic f/h contours (to within a factor $|\nabla\frac{f}{h}|$) and the so-called Joint Effect of Baroclinicity and Relief (JEBAR, Sarkisyan and Ivanov (1971)). The former is the vorticity of the depth-averaged Coriolis force. It can be decomposed into:

$$J\left(\Psi, \frac{f}{h}\right) = \beta\frac{V}{h} + f\frac{\mathbf{U_h}}{h}\cdot\frac{\nabla_h h}{h} \quad (13)$$

The first right hand side term is the beta effect, identically to Equations 4 and 10 to within a factor $\frac{1}{h}$. The second rhs term is the so-called topographic beta effect resulting from diagnosing vertically-averaged forces. The last term of Equation 12 is the vorticity of the depth-average baroclinic pressure force. It can be interpreted as the baroclinic torque of the force exerted by the fluid normal to solid Earth (Mertz & Wright, 1992) by integrating Equation 7 vertically, giving:

$$hP_b = <P> + \chi \quad (14)$$

and expressing:

$$\frac{1}{\rho_0}J(P_b, h) = \frac{1}{\rho_0}\mathrm{Curl}(P_b\nabla_h h) = \frac{1}{\rho_0}\left(\frac{1}{h}J(<P>, h) + hJ\left(\chi, \frac{1}{h}\right)\right) \quad (15)$$

where we have again neglected the free surface height given $\eta \ll h$.

The third entry of Table 1 summarizes the main properties of this balance. Equation 12 involves transports in relation with geostrophic contours. It provides a diagnostic balance for transport across those contours. It is particularly appealing to barotropic models because in this case $\chi = -g^*\rho_0\frac{h^2}{2}$ and JEBAR cancels out. Therefore barotropic flows are strongly attached to geostrophic contours (LaCasce & Isachsen, 2010; Patmore et al., 2019). However, the flow baroclinicity mitigates this constraint by generally weakening at depth, the JEBAR term tending to detach the flow from those contours. Geostrophic contours are a fixed external forcing for the flow, so that insightful properties of the circulation can be deduced solely from their geometry (Olbers et al., 2004). Equation 12 can be divided by either $h\,|\nabla\frac{f}{h}|$ or $|\nabla\frac{f}{h}|$ to obtain a diagnostic equation for the depth-average velocities or the transports across geostrophic contours.

We illustrate again this balance in a northern subtropical gyre assuming geostrophic and surface Ekman dynamics (Figure 1c). In the interior ocean, the Sverdrup balance becomes a topographic Sverdrup balance in the presence of topography. If the flow were purely barotropic, it would be allowed to only marginally deviate from geostrophic f/h contours to the extent that the wind stress curl permits it. However, the flow is largely baroclinic with weakened velocities at the bottom. As a consequence, the JEBAR effect decouples the flow from the bottom topography and allows it to cross topographic obstacles. Along the western boundary, the situation is similar: the larger the baroclinicity, the higher the deviation of the depth-averaged flow from geostrophic contours and the less relevant the topographic Sverdrup balance.

2.6. Transport Divergence Vorticity Balance

The fourth depth-integrated vorticity balance is obtained by taking the curl of Equation 9 divided by f, yielding:

$$\mathrm{Curl}\left(\frac{\partial \mathbf{U_h}/f}{\partial t}\right) = \mathrm{Curl}\frac{<\mathbf{A}>}{f} + \mathrm{Curl}\frac{<\mathbf{D}>}{f} + \frac{1}{\rho_0}\mathrm{Curl}\left(\frac{\tau_s - \tau_b}{f}\right) + \frac{1}{\rho_0}\left(J\left(P_b, \frac{h}{f}\right) + J\left(\chi, \frac{1}{f}\right)\right) \quad (16)$$

which is only defined outside of the Equator. Again, we have neglected horizontal variations of the free surface, given that $\eta \ll h$, so that the sea level contribution to the bottom pressure-driven transport convergence

$\frac{1}{\rho_0} J\left(P_b, \frac{\eta}{f}\right)$ can be neglected. All the right hand side terms of this equation can be interpreted as force-driven integral transport convergences, the sum of which must approximately cancel out by mass conservation. Consistently, the Coriolis force vanishes when deriving Equation 16. The frictional term is the convergence of the surface plus bottom Ekman transports, or equivalently the surface plus bottom Ekman pumping:

$$\frac{1}{\rho_0}\mathrm{Curl}\left(\frac{\boldsymbol{\tau_s} - \boldsymbol{\tau_b}}{f}\right) = \frac{1}{\rho_0}(w_{Es} - w_{Eb}) \tag{17}$$

with w_{Es} and w_{Eb} the surface and bottom Ekman vertical velocities. As already documented in numerous studies (e.g., Yeager, 2015), the Ekman pumping is mostly driven by the frictional stress curl, whereas the Ekman beta effect related to f variations plays a marginal role away from the Deep Tropics (Pedlosky, 1996). The last two terms are the convergence of the bottom pressure-driven geostrophic transport and that of the baroclinic pressure-driven geostrophic transport. The former is the integral of a barotropic (depth-independent) transport increasing with h (the depth-integral is larger) and decreasing with f (less transport is needed for the Coriolis force to balance pressure forces at higher latitudes). Therefore it diverges (resp. converges) if h/f increases (resp. decreases) along P_b contours leaving high pressures to the right. The latter term is the integral of a baroclinic (depth-dependent) transport independent of h (implicitely incorporated in gradients of χ) but also decreasing with f. In this case, only meridional baroclinic transports driven by zonal gradients of χ can diverge as a consequence of the beta effect. Finally, nonlinear advection and dissipation (first and second right hand-side terms of Equation 16) also force a transport divergence if they have a torque or if their zonal component is non-zero, as a result of the beta effect.

The fourth entry of Table 1 summarizes the main properties of this balance. Equation 16 is almost absent from the oceanographic litterature. To our knowledge, it is only expressed and briefly interpreted by Hughes and Killworth (1995). However, the underlying dynamics are very familiar to physical oceanographers: it is a depth-integrated mass conservation equation expressed in terms of the dominant large-scale forces. Innumerable studies have designed hydrographic sections to estimate lateral transports at the boundaries of an oceanic control volume in terms of Ekman plus geostrophic dynamics (e.g., Ganachaud & Wunsch, 2000). This is a particular case of Equation 16 integrated over a finite volume and simplified assuming only the surface frictional stress (third rhs term of Equation 16) and bottom plus baroclinic pressure forces (last two terms of Equation 16) are non-zero.

We illustrate again this balance in a northern subtropical gyre assuming geostrophic and surface Ekman dynamics (Figure 1d). In both the interior ocean and the western boundary, the situation is identical: the anticyclonic wind stress curl causes an Ekman convergence. To ensure mass conservation, a geostrophic transport divergence must prevail. This can be done by the increase of bottom pressure along geostrophic f/h contours, or through the increase of baroclinic potential energy at constant latitude (along f contours).

Vorticity Equations 4, 10, 12, and 16 are the simplification of a three-dimensional dynamical balance. By vertically-integrating, we focus on the forces and flows in the horizontal plane and we lose information on their vertical distribution. However, the flow adjusts vertically and ocean sublayers are dynamically coupled to satisfy at all time those barotropic constraints. We have highlighted in particular the key role of bottom boundary conditions in the setting of BV balances. Bottom pressure, bottom vertical velocities and bottom friction are internal properties of the fluid in the sense that they result from the three-dimensional adjustment of mass and motion. On the contrary, the surface frictional stress is essentially an external forcing driven mostly by near-surface wind (Fairall et al., 2003; Renault et al., 2017). In both cases, ocean circulation must adjust vertically to balance those internal and external forcings. We show in Appendix A5 that depth-dependent counterparts can be formulated for the vorticity Equations 4, 10, 12, and 16, highlighting the role of vorticity redistribution through the generation of vertical motion. In what follows, we will restrict the analysis to the four depth-integrated vorticity balances introduced in this section.

3. Discretization in an Ocean Climate Model

3.1. A Global Ocean Climate Configuration

In what follows, we aim at diagnosing the momentum and vorticity balances established in Section 2 in the ocean component of a climate model participating in the sixth Climate Model Intercomparison Program (CMIP6,

Eyring et al. (2016)). We analyze years 1900–2399 of a pre-industrial control re-run of the CNRM-CM6 climate model for which all terms of the zonal and meridional momentum equations have been stored online. This model was recently described and evaluated by Voldoire et al. (2019). It includes the atmospheric model ARPEGE-Climat (Voldoire et al., 2013) coupled via the OASIS coupler (Craig et al., 2017) to the SURFEX land surface model (Decharme et al., 2019), the NEMO version 3.6 ocean model (Madec, 2008) and the imbedded GELATO sea ice model (Chevallier et al., 2013). Horizontal resolutions are 1.4° over the spectral atmospheric and land surface grid, and the nominal 1° resolution over the ocean and sea ice tripolar curvilinear ORCA grid. The atmospheric component has 91 vertical levels and the ocean component has 75 levels (resolution from 1 m at surface to 200 m at deepest levels). The main ocean physical parametrizations are the turbulent kinetic energy prognostic scheme for vertical turbulence (Blanke & Delecluse, 1993), the enhanced vertical diffusion scheme for convection (Madec, 2008), the mesoscale and submeso-scale isoneutral mixing (Redi, 1982) and eddy-induced velocities (Fox-Kemper et al., 2008; Visbeck et al., 1997) for tracers, and the tidal mixing parametrization of de Lavergne et al. (2016, 2019). In this pre-industrial simulation, external forcings (solar, greenhouse gases and aerosols) are kept constant to their estimated value of year 1850. A 350-year spin-up has been performed prior to the analyzed period and ensures an equilibration of net air-sea heat fluxes at 0.15 W/m^2, equivalent to a surface drift of 0.02 K per century. In what follows, we exclusively analyze physical parameters related to the horizontal momentum (and derived vorticity) equations, namely: all the terms of the zonal and meridional momentum tendency equations, horizontal velocities and surface wind stress. We propose a climatological mean view of each balance, so that only the 500-year averages over the whole period are analyzed. The main results are unchanged when considering yearly averages over the period (not shown).

3.2. The VoBiN Diagnostic Vorticity Package for NEMO

All momentum and vorticity equations introduced in Section 2, discretized in this section and illustrated in the next section have been coded in the Vorticity Balances in NEMO (VoBiN) package, freely available at github.com/RobinWaldman/VoBiN. They are designed for NEMO configurations with time-splitted momentum equations and the Energy and Enstrophy (EEN) conserving Coriolis scheme (see below for details), and could serve as a basis for further extension to other configurations and numerical C-grid ocean models (Mesinger & Arakawa, 1976). This package extends the work of Styles et al. (2022) who focused exclusively on the discretization of the BV Equation 10. The only required input parameters are: the terms of the zonal and meridional momentum equations, horizontal velocities, surface wind stress and the model mesh and mask parameters. We detail below how the most crucial discretization issues for those equations are dealt with in the VoBiN package.

3.3. Model Discretizations

As will be shown in the next section, details of the model discretization play a leading-order role in the modeled vorticity balances. In Appendix B1, we discuss the limited time discretization issues. Spatially, the NEMO model is formulated in the so-called Arakawa-C grid (Mesinger & Arakawa, 1976), for which u-velocity and v-velocity points are apart from each other (see Figure 2). As we will see, this has profound consequences for the vorticity of the discretized Coriolis force.

3.3.1. Discretized Vorticity Balances in the C-Grid

In ocean modeling, the two most common finite difference grid formulations are the B-grid (e.g., MOM5, POP) and the C-grid (e.g., HYCOM, MITGCM, MOM6, NEMO, ROMS). In the B-grid, u and v velocity points are both located at the northeastern corner of each cell (Arakawa & Lamb, 1977). Conversely, in the C-grid, u velocity points are located at the eastern face of each cell, whereas v velocity points are at the northern face (see Figure 2). As a consequence, the invariant curvilinear formulation for the Curl of horizontal momentum trends writes in NEMO as:

$$\mathrm{Curl}(utrd, vtrd) = \frac{1}{e1f\ e2f}\left(\delta_{i+1/2}(vtrd\ e1v) - \delta_{j+1/2}(utrd\ e2u)\right) \tag{18}$$

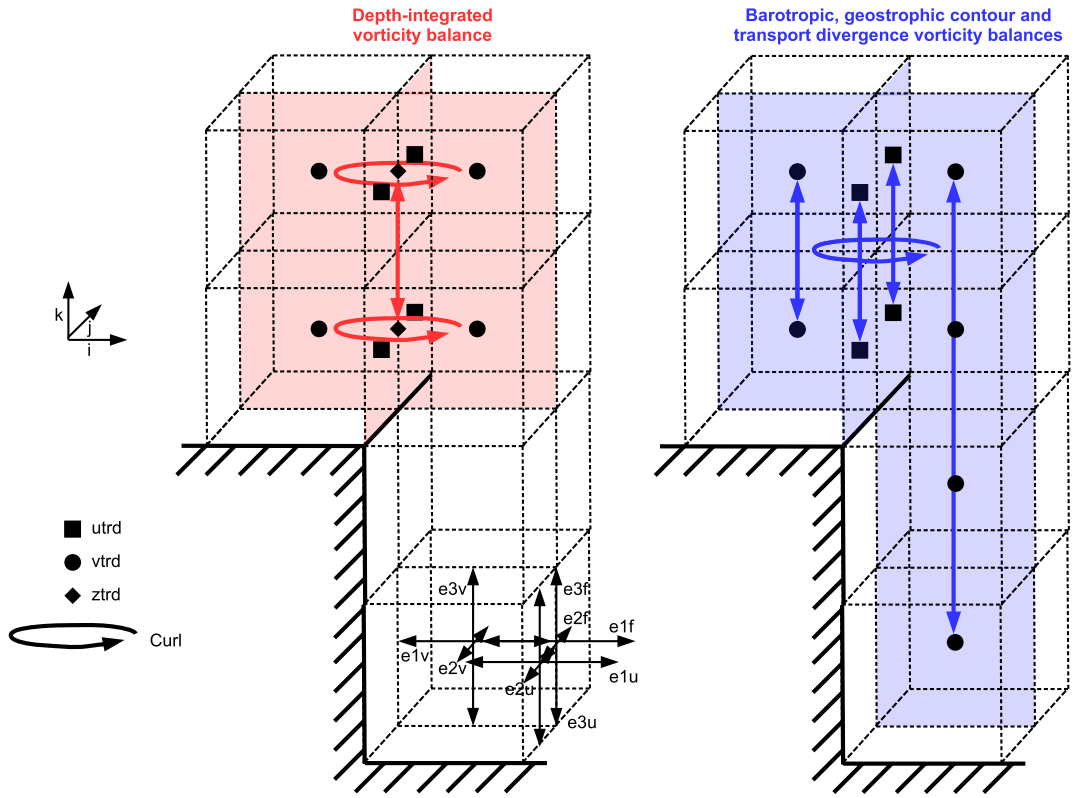

Figure 2. Vorticity balances in the NEMO model under the curvilinear Arakawa-C grid discretization. Zonal (resp. meridional) velocities and forces are located at the eastern (resp. northern) face of each grid cell, on the so-called u-grid (resp. v-grid). As a result, vorticity trends are located at the northeastern corner of each cell, on the so-called f-grid. The depth-integrated vorticity balance includes all f-points for which the two neighboring u and v-points are non-zero, hence going down to the top of the bathymetry (red shading). Vorticity balances derived from the depth-integrated momentum equation include all non-zero u-points and v-points, hence going deeper in the water column (blue shading). On the bottom, horizontal and vertical grid scale factors are illustrated on each of the momentum and vorticity grid locations.

with e1f, e2f, e1v, and e2u the i and j-direction horizontal scale factors on the f-grid, v-grid and u-grid (see Figure 2 for their location and orientation), $\delta_{i+1/2}\, x = x(i+1, j, k) - x(i, j, k)$ and $\delta_{j+1/2}\, x = x(i, j+1, k) - x(i, j, k)$ with k the vertical index. The vorticity of the depth-integrated momentum trends writes as:

$$\mathrm{Curl}\left(\int_{-h}^{0} utrd\, dz, \int_{-h}^{0} vtrd\, dz\right) = \frac{1}{e1f\, e2f}\left(\delta_{i+1/2}\left(e2v \sum_{k} vtrd\, e3v\right) - \delta_{j+1/2}\left(e1u \sum_{k} utrd\, e3u\right)\right) \quad (19)$$

with $\sum_k$ the vertical full-depth summation, e3v and e3u the v-grid and u-grid vertical scale factors (see Figure 2).

A crucial aspect of the vorticity equation analysis in a numerical model with geopotential vertical coordinates is the way lateral boundary conditions are dealt with. In our NEMO configuration, we use a no-slip lateral boundary condition, meaning that at the land boundary, velocities tangent to the solid boundary are null. However, we do not have any explicit condition on individual forces at those boundaries. If we assume that all momentum trend contributions are also zero, large and compensating vorticity trends are generated with no transport signature. In the perspective of interpreting oceanic transports, this choice is irrelevant. Therefore, all lateral boundaries are masked and excluded from the vorticity analysis.

We obtain the discretized depth-integrated vorticity balances illustrated in Figure 2. All vorticity balances are defined in the f-grid, that is at the northeastern corner of each cell. For the depth-integrated vorticity balance (red symbols in Figure 2), depth integration goes down to the bottommost f-grid point for which all neighboring u and v-points are non-zero. As a consequence, a few oceanic u and v-points (blue squares and circles in Figure 2) near the bottom are excluded from the analysis. In particular, the bottom stress curl is evaluated above the topographic boundary layer, and the bottom vortex stretching is induced by the bottommost non-zero vertical velocity on the

f-grid, that is again above the topographic boundary layer (bottommost red diamond in Figure 2). On the contrary, vorticity balances deduced from the depth-integrated momentum equation include all non-zero u and v-points, with no bottom cell exclusion (blue arrows in Figure 2). In that sense, they correspond to the vorticity balances of the model's full momentum equations. In particular, the bottom stress curl is evaluated at the bottommost oceanic cells (bottommost blue squares and circles in Figure 2) and the bottom pressure torque is the pressure force per unit grid width integrated over f-grid points next to side walls (blue circles next to land in Figure 2). These differences are a discretized form of the Leibniz integration formula expressed in Equation 11. Both balance formulations are identical in the case of a flat bottom or if momentum trends cancel out near the topography.

3.3.2. Discretized Coriolis Force

We now turn to discretization issues related to the Coriolis force. In the so-called B-grid, formulating the Coriolis force is straightforward, however the pressure force requires a double averaging which is error prone. Reversely, in the C-grid, formulating the pressure force is straightforward, however the Coriolis force requires again a double averaging in order to interpolate u onto the v-grid, and v onto the u-grid. Next to land points, this interpolation is particularly error prone.

In Appendix B, we develop the discretized expression for the Coriolis force (Appendix B1), its vorticity (Appendix B2) and the vorticity of its depth-integral under the most widespread Energy and Enstrophy (EEN) conserving scheme in the NEMO model. We show that a numerical beta effect arises from modifications of the Coriolis parameter under discretized Coriolis schemes, and a numerical vortex stretching appears from the interpolation of u velocities onto the v-grid (and conversely) which is inherent to C-grid models. Given the linearity in time of the Coriolis force, they can be properly decomposed offline from the knowledge of horizontal velocities and the model grid scale factors. While the numerical beta effect can be mitigated by alternative discretization schemes, the numerical vortex stretching is intrinsic to C-grid ocean models, especially with a geopotential vertical coordinate which increases the lateral boundary area with solid Earth. Our results are in line with those of Styles et al. (2022) who only diagnosed the discretized BV Equation 10. Here we further propose a discretized decomposition for the depth-dependent Coriolis force (Appendix B2), its vorticity (Appendix B3) and the three extra depth-integrated Coriolis torques deduced from the vorticity Equations 4, 12, and 16 (Appendix B4). As we show in the next section, those discretization issues have large consequences on the model vorticity balances.

4. Dynamical Balances of an Ocean Climate Model

In this section, we diagnose in the CNRM-CM6 climate model all the vorticity equations developed above and coded in the VoBiN diagnostic package to highlight two fundamental aspects of ocean models' dynamical balances: topographic constraints, and numerical effects. For simplicity, we focus on their zonal integral along three zonal cross-sections of the subpolar, subtropical and equatorial Atlantic Ocean. For an analysis of the full global maps of the model's depth-integrated momentum and vorticity balances, see the Texts S1, S2, and S4–S6 in Supporting Information S1, respectively.

4.1. Depth-Integrated Vorticity Balance

Figure 3 shows the depth-integrated vorticity trends (Equation 4 discretized by depth-integrating Equation 18), zonally integrated from the eastern boundary, along three zonal sections of the subpolar, subtropical and equatorial Atlantic Ocean. By construct, the beta term equals the zonal integral meridional transport (in *Sv*), to within a factor β and 4-point averaging inherent to C-grid discretization (see Appendix B3), and is balanced by the sum of the remaining terms. At 50°N, we identify a southward western boundary flow of 20 Sv west of 43°W, corresponding to the Labrador Current, and a northward flow of 20 Sv between 35 and 15°W corresponding to the North Atlantic Current (Figure 3a). The former is balanced by a large bottom vortex stretching (20 Sv) and to a lesser extent by bottom stress (3 Sv), while the dissipative, wind stress and numerical torques oppose it by 2 Sv, 2 Sv, and 1 Sv, respectively. The latter is balanced by a combination of dissipation (10 Sv), bottom vortex stretching (5 SV) and wind stress curl (5 Sv), the other terms being second-order. The subpolar vorticity balance is therefore largely topographic, and to a lesser extent wind-driven and viscous.

At 30°N, we identify a northward western boundary flow of 33 Sv west of 76°W, corresponding to the Gulf Stream, and an interior southward return flow of 40 Sv east of that longitude (Figure 3b). Note that the net zonal integral does not exactly conserve mass because of the horizontal averaging inherent to the model C-grid, on top

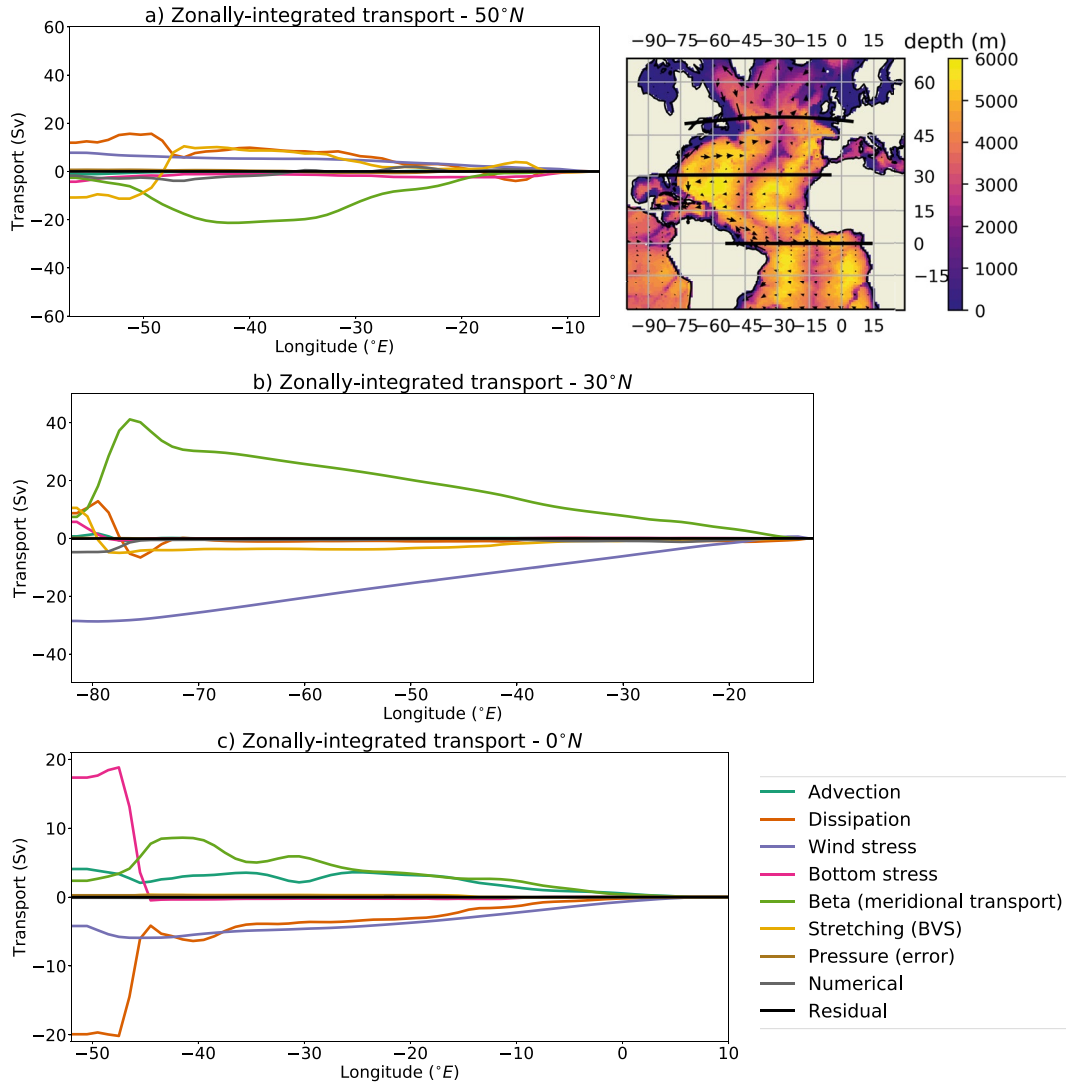

Figure 3. Depth-integrated vorticity equation in the (a) subpolar, (b) subtropical and (c) equatorial Atlantic Ocean, zonally integrated from the eastern boundary and divided by β to be expressed as meridional transports, in *Sv*. Terms follow Equation 4, with BVS standing for bottom vortex stretching, the pressure term being a numerical error and the residual containing the total trend and unaccounted for numerical errors. The top right map shows the location of each zonal section (black lines), the bathymetry (shades) and depth-integrated horizontal transports (arrows).

of the small mass imbalance driven by the surface mass budget. The northward flow is balanced by a combination of bottom vortex stretching (17 Sv), dissipation (17 Sv) and bottom stress (6 Sv), while the numerical torque opposes it by 5 Sv. The interior flow is overwhelmingly balanced by wind stress curl (30 Sv), with a small contribution of dissipation (5 Sv) and bottom stretching (4 Sv), the other terms being second-order. The subtropical vorticity balance is therefore mostly viscous and topographic at the western boundary and wind-driven in the interior.

Along the Equator, we identify a northward western boundary flow of 6 Sv west of 42°W, corresponding to the North Brazil Current, and an interior southward return flow of 8 Sv east of that longitude (Figure 3c). The northward flow is overwhelmingly balanced by bottom stress (18 Sv), itself largely compensated by dissipation (14 Sv), with a second-order contribution of nonlinear advection (1 Sv) and wind stress (1 Sv). The southward return flow is balanced by wind stress curl (5 Sv) and dissipation (5 Sv), with a small compensation by nonlinear advection (3 Sv). The Equatorial vorticity balance is therefore bottom stress-driven along the western boundary and both wind and dissipation-driven in the interior.

Overall, the depth-integrated vorticity equation shows the relevance of topographic effects at subpolar latitudes and along western boundaries, in agreement with Hughes and de Cuevas (2001). Numerical effects are nonnegligible but they largely remain second-order, at odds with results from Styles et al. (2022) based on the BV equation. As will be shown below, this is due to the exclusion of bottom grid cells inherent to the discretization procedure for the depth-integrated vorticity equation (see Figure 2). In addition, we find a large wind stress forcing in the interior, consistently with Sverdrup theory, although it accounts for a small fraction of the total transport at subpolar latitudes. Dissipative effects are large along western boundaries, but also non-negligible in the interior along the Equator and in the subpolar north Atlantic. Along western boundaries, Munk theory provides an interpretation in terms of balancing of the beta effect by the viscous torque caused by land-sea lateral interaction (Munk, 1950). Recent studies have shown that this behavior is specific to low-resolution models while at higher resolution, western boundary currents are largely inviscid and balanced by inertial and topographic torques (e.g., Hughes & de Cuevas, 2001). We can also note that the staircase formulation of z-level models, with a viscous torque next to vertical side walls, is at odds with a mostly sloping bottom. Instead, recent work with a high-resolution sigma-coordinate model has shown that the bottom drag curl becomes a leading-order term of the balance near lateral boundaries (Le Corre et al., 2020). Finally, bottom friction and nonlinear effects are only significant along the Equator.

Text S2 in Supporting Information S1 provides a global view of the depth-integrated vorticity equation. It confirms the above interpretation with a mixture of topographic, viscous and numerical effects at mid-high latitudes and along boundaries, a mostly Sverdrupian balance in the interior of subtropical and tropical gyres, and significant nonlinear effects within 5° of the Equator. Furthermore, Text S3 in Supporting Information S1 provides a zonal Atlantic cross-section of the depth-dependent vorticity equation (Equation A13, see Appendix A5) at 50°N. It shows that depth-integrated vorticity balances largely result from the generation of vertical motion by the surface (frictional) and bottom (topographic and numerical) boundary layers, coupled to the interior ocean through interior vortex stretching.

4.2. Barotropic Vorticity Balance

We now turn to the barotropic vorticity (BV) balance (Equation 10 discretized by Equation 19). Its discretized form in the NEMO model has already been extensively analyzed by Styles et al. (2022) in an idealized gyre configuration and an eddying global ocean simulation. Here we complement their analysis with an ocean climate simulation and provide a comparison to the alternative depth-integrated vorticity equation analyzed above. We have seen in Sections 2 and 3 that, although it bears many similarities with the depth-integrated vorticity equation, this balance is more comprehensive in the sense that it includes all the model momentum points. From an analysis point of view, it also has the convenience of including only one physical torque for the Coriolis force, namely the beta effect, when neglecting the Goldsbrough-Stommel effect. However, we will show here that the depth-integrated vorticity equation is less prone to spurious torques.

Figure 4 shows the BV trends, zonally integrated from the eastern boundary, along three zonal sections of the subpolar, subtropical and equatorial Atlantic Ocean. We find the same terms as in Figure 3, with three notable exceptions: the bottom pressure torque now replaces the physical bottom vortex stretching as a topographic effect, the Goldsbrough-Stommel effect is non-zero and all terms are integrated throughout the full water column before cross-differentiation. As a consequence, the physical beta effect, the inertial, bottom stress and dissipative torques are close to those of Figure 3, only differing due to the inclusion of a few extra grid cells near the topography (see Figure 2), where velocities are generally weak. The physical beta effect (and associated transport) is almost unchanged along the equatorial and subpolar north Atlantic, while being weakly increased in the subtropics, with a northward flow of 39 Sv and a southward return flow of 42 Sv. The inertial torque is increased in all sections. It however only becomes a significant forcing for the northward equatorial flow, with a transport of 4 Sv. The bottom stress is actually reduced because as illustrated in Figure 2, it is now evaluated at the bottom-most grid cells where it is weaker, as are velocities. It however remains the dominant forcing for the Equatorial western boundary flow, with a transport of 13 Sv. The dissipative torque bears again many similarities in both balances, being mostly unchanged at subpolar latitudes and modestly reduced in the subtropics and along the Equator. The wind stress curl contribution is identical in both balances to the extent that horizontal sea level variations can be neglected in the torque of the surface wind stress, as discussed in Section 2. The Goldsbrough-Stommel effect is weak, only compensating for 3 Sv of the northward subtropi-

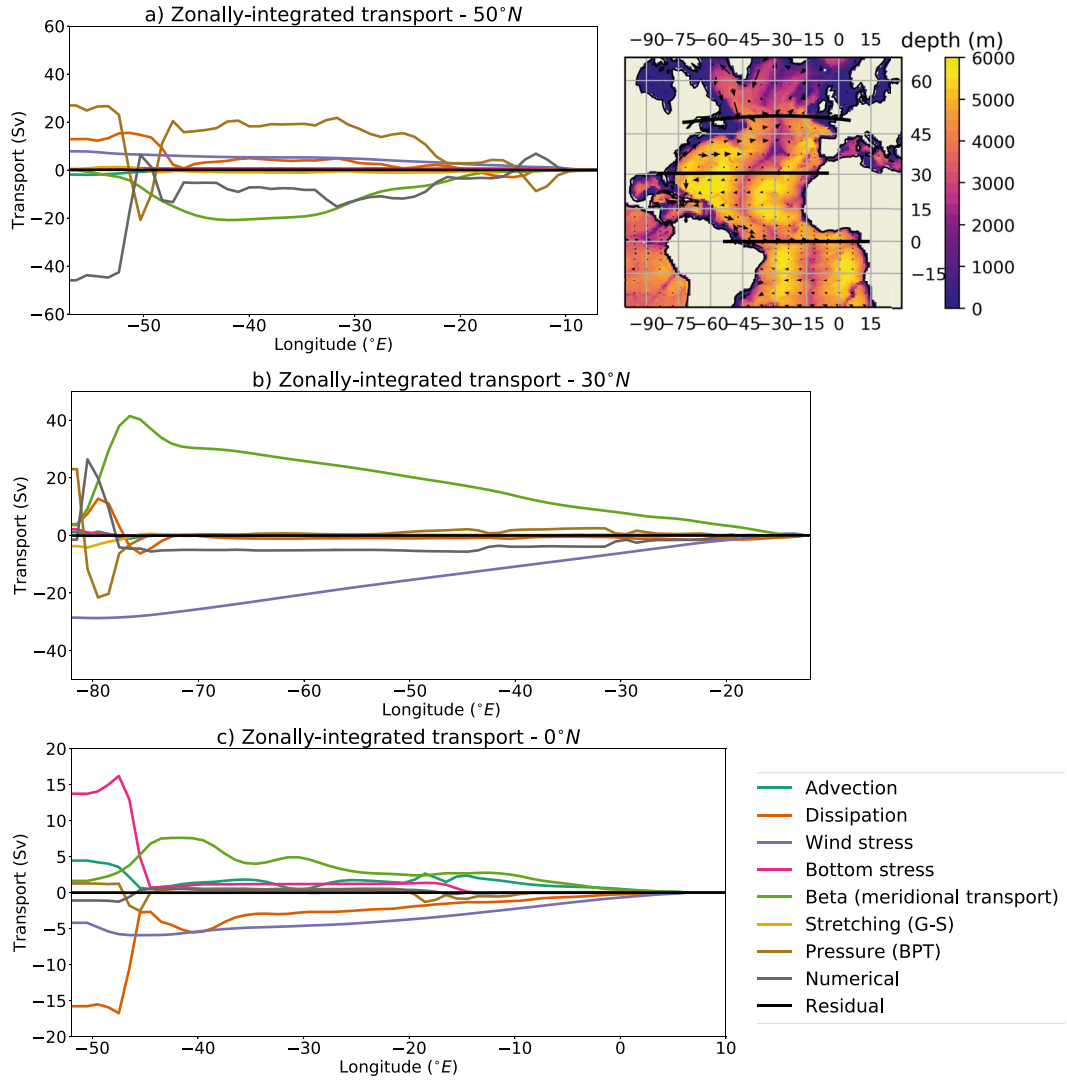

Figure 4. Barotropic vorticity equation in the (a) subpolar, (b) subtropical and (c) equatorial Atlantic Ocean, zonally integrated from the eastern boundary and divided by β to be expressed as meridional transports, in *Sv*. Terms follow Equation 10, with G-S standing for the Goldsbrough-Stommel circulation, BPT the bottom pressure torque and the residual containing the total trend and unaccounted for numerical errors. The top right map shows the location of each zonal section (black lines), the bathymetry (shades) and depth-integrated horizontal transports (arrows).

cal flow. However, the most spectacular difference between both balances concerns the bottom pressure and numerical topographic torques. The former generally largely differs from the bottom vortex stretching, with overall larger values, hence indicating strong topographic torques over the bottom-most grid cells. The latter exceeds by one to two orders of magnitude that of the depth-integrated vorticity equation. It becomes dominant in the subpolar section and along the subtropical western boundary. This numerical torque is largely dominated by the numerical vortex stretching caused by the masking of u and v velocities inherent to the C-grid (see developments in). As a consequence, the momentum equations feel a large transport divergence near the topography which causes an intense topographic torque. Figure 4 tells us that the model mostly balances this numerical torque through the bottom pressure torque, that is through mass adjustments near the bottom. The main consequences in terms of vorticity balances are that: the southward subpolar flow is now forced by the numerical torque and compensated by dissipation and bottom pressure (Figure 4a); and both the northward subpolar and subtropical flows, which are largely bottom pressure-driven, are now partially compensated by the numerical torque (Figures 4a and 4b).

Overall, the BV balance confirms limitations of the Sverdrup theory and the key constraint posed by topography on the flow near boundaries and over subpolar latitudes. It also highlights large numerical topographic torques arising from the discretization of the Coriolis force in C-grid ocean models such as NEMO, in line with previous results by Styles et al. (2022). Those results are confirmed by the global BV balance analysis of Text S4 in Supporting Information S1, showing that the numerical torque is significant over most mid-high latitude regions and along boundaries. They put into question the current modeling approaches which are likely to affect the depth-integrated flow. From a model analysis perspective, the depth-integrated vorticity Equation 4 has the advantage of retaining most of the meridional flow and containing limited numerical torques, contrary to the BV Equation 10 analyzed here and in Styles et al. (2022).

4.3. Geostrophic Contour Vorticity Balance

Figure 5 shows the geostrophic contour vorticity trends (Equation 12 discretized by the depth-average analog of Equation 19), zonally integrated from the eastern boundary, along three zonal sections of the subpolar, subtropical and equatorial Atlantic Ocean. By construct, the beta term equals the transport across geostrophic contours (in *Sv*), to within a factor $|\nabla \frac{f}{h}|$, and is balanced by the sum of the remaining terms. Transport across geostrophic contours is largely dominated in the subpolar section by the North Atlantic Current crossing of the mid-Atlantic ridge, centered at 29°W (Figure 5a). It is mostly balanced by the baroclinic pressure torque, namely JEBAR, and to a lesser extent by dissipation east of 30°W, with the numerical torque partially compensating both forcings. The remaining terms are second-order.

In the Subtropics, transport across geostrophic contours is highest along the western boundary, corresponding to the Gulf Stream crossing of the western boundary slope, and significant around 42°W where the southward flow crosses the mid-Atlantic ridge (Figure 5b). The former is balanced by the JEBAR and numerical topographic torques, with a weak effect of the Goldsbrough-Stommel term. The latter is dominated by the numerical torque, with a weak effect of JEBAR and wind stress. Throughout the interior, a weak negative transport is forced by wind stress and to a lesser extent JEBAR and the numerical torque.

Along the Equator, transport across geostrophic contours is larger along the western boundary, west of 42°W, than in the interior, due to the North Brazil Current flow over sloping topography (Figure 5c). The former is again largely driven by bottom friction, with a weak contribution from nonlinear advection and a large compensation by wind stress, dissipation and JEBAR. In the interior, the weak negative transport is driven by wind stress and dissipation, with a weak compensation by JEBAR, nonlinear advection and bottom stress.

Overall, the geostrophic contour vorticity equation tells us that the topographic constraint is not as large as suggested by barotropic models. Indeed, modest values of the wind stress forcing away from the Equator invalidate the barotropic theory of topographic Sverdrup balances which states that the wind stress is the main forcing allowing the flow to cross geostrophic contours (e.g., LaCasce & Isachsen, 2010). As illustrated in Figure 1c, the JEBAR term tells us that the flow is sufficiently baroclinic to circumvent topographic obstacles. In other words, the flow is sufficiently surface-intensified and weak at depth to be decoupled from topography and cross bottom seamounts and slopes, particularly at subpolar latitudes and along western boundaries. In addition, this balance puts again into question the realism of C-grid ocean models which produce large numerical topographic torques that are likely to affect the circulation. They are largely dominated by the numerical beta effect, namely the numerical transport across the model's geostrophic contours f_{EEN}/h (see Appendix B). Because of numerical modifications of the Coriolis parameter, the modeled ocean circulation crosses artificial geostrophic contours, which poses an extra topographic constraint to the flow. This constraint is largely balanced both by transports across actual geostrophic contours (the physical beta effect) and the baroclinicity of the flow (the JEBAR pressure term). Text S5 in Supporting Information S1 provides a global view of the geostrophic contour vorticity equation, confirming the driving role of the flow baroclinicity and thus limitations of barotropic models of the ocean circulation.

4.4. Transport Divergence Vorticity Balance

Figure 6 shows the transport divergence vorticity trends (Equation 16 discretized by the transport analog of Equation 19), zonally integrated from the eastern boundary, along three zonal sections of the subpolar, subtropical

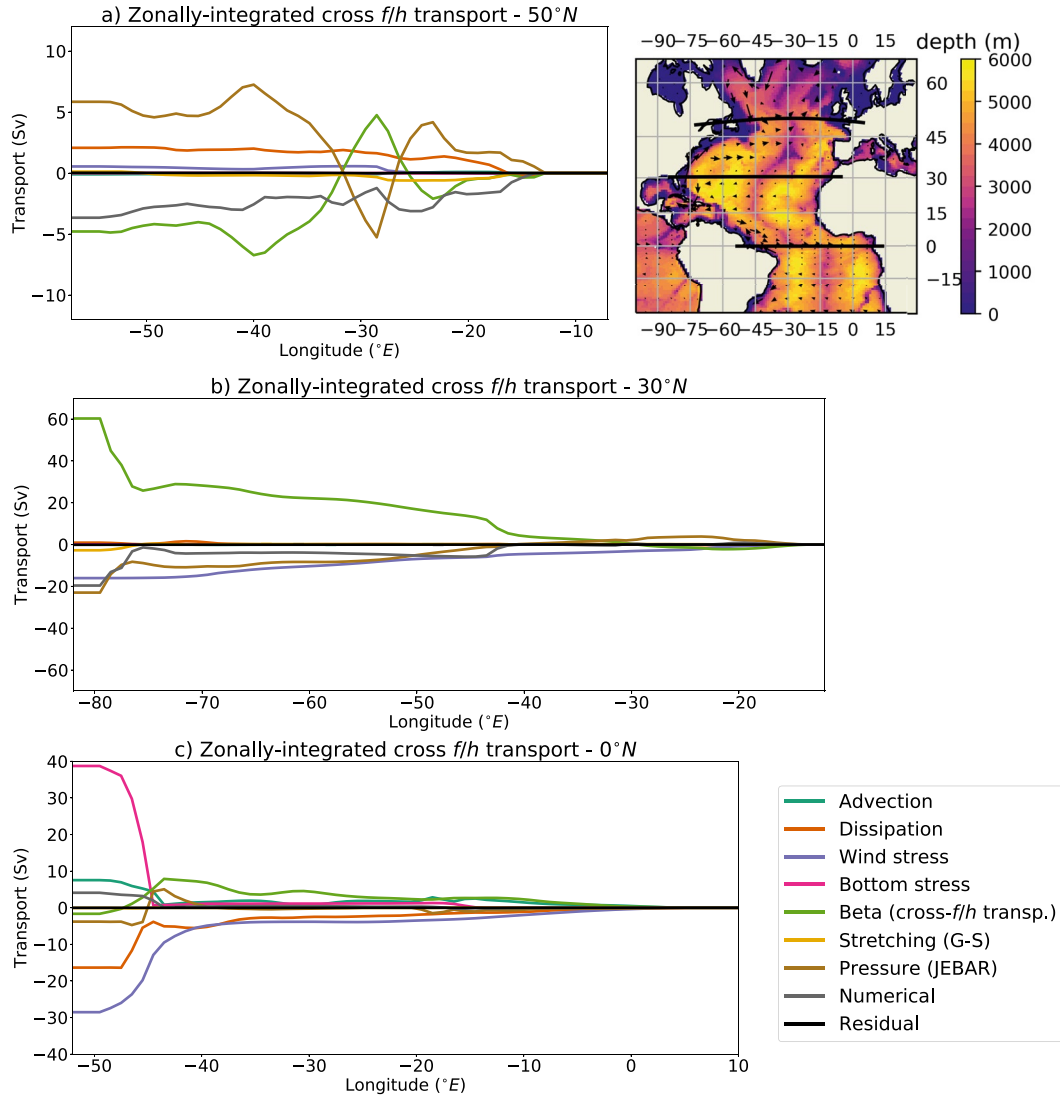

Figure 5. Geostrophic contour vorticity equation in the (a) subpolar, (b) subtropical and (c) equatorial Atlantic Ocean, zonally integrated from the eastern boundary and divided by $|\nabla \frac{f}{h}|$ to be expressed as transports across geostrophic contours, in *Sv*. Terms follow Equation 12, with G-S standing for the Goldsbrough-Stommel circulation, JEBAR the joint effect of baroclinicity and relief and the residual containing the total trend and unaccounted for numerical errors. The top right map shows the location of each zonal section (black lines), the bathymetry (shades) and depth-integrated horizontal transports (arrows). A 5-point running window has been applied to h prior to $|\nabla \frac{f}{h}|$ computation to reduce grid-scale noise.

and equatorial Atlantic Ocean. By construct, the stretching term equals the depth-integrated transport divergence (in m^2/s), and its near-zero value is balanced by the sum of the remaining terms. In the subpolar section, west of 47°W, a strong numerical convergence is balanced by geostrophic and to a lesser extent viscous divergence (Figure 6a). East of that longitude, a significant Ekman pumping is balanced by numerical convergence, itself largely compensated by geostrophic convergence.

In the subtropical section, along the western boundary, strong compensation occurs between numerical convergence and geostrophic divergence (Figure 6b). Overall, west of 76°W, a small transport divergence is balanced by the viscous torque and compensated by geostrophic divergence. In the interior ocean, the balance is largely driven by Ekman suction and geostrophic divergence, consistently to the schematic of Figure 1d. In addition, a small numerical convergence is balanced by geostrophic divergence.

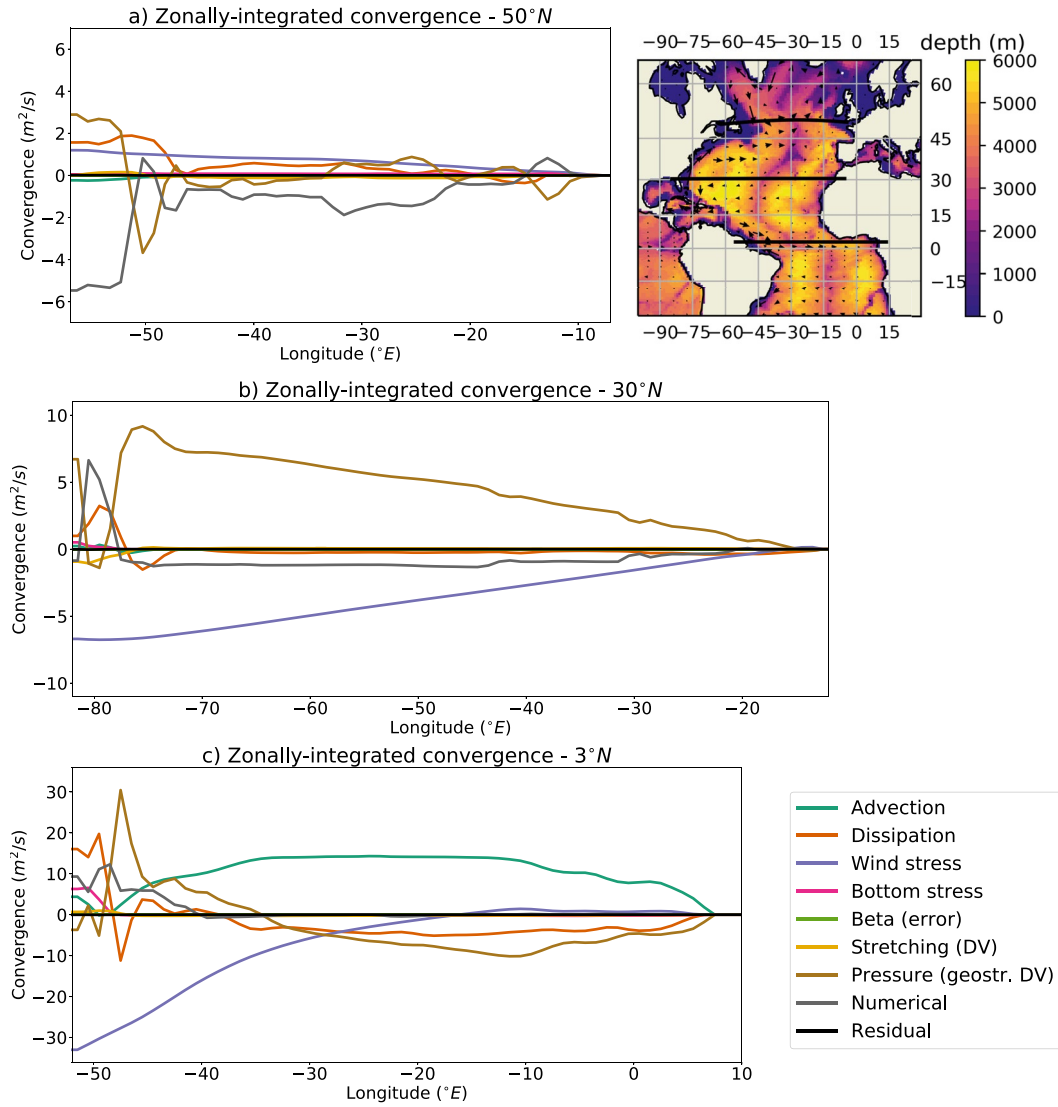

Figure 6. Transport divergence vorticity equation in the (a) subpolar, (b) subtropical and (c) equatorial Atlantic Ocean, zonally integrated from the eastern boundary (in m^2/s). This balance being undefined along the equator, the equatorial section is evaluated at 3°N. Terms follow Equation 16, with the beta term being a numerical error, DV standing for the net depth-integrated transport divergence, the pressure term corresponding to the geostrophic divergence and the residual containing the total trend and unaccounted for numerical errors. The top right map shows the location of each zonal section (black lines), the bathymetry (shades) and depth-integrated horizontal transports (arrows).

In the Equatorial section at 3°N, the weakness of the Coriolis force leads to large convergences of individual torques (Figure 6c). This implies that much larger transports are required for the Coriolis force to balance other terms of the momentum equations. Along the western boundary, west of 45°W, a large geostrophic convergence and Ekman suction is balanced by dissipative divergence and to a lesser extent bottom stress and numerical torques. Over the interior, west of the Gulf of Guinea (10°W), a large Ekman suction and weaker nonlinear convergence are balanced mostly by geostrophic divergence and to a lesser extent viscous and numerical divergence. Finally, within the Gulf of Guinea (east of 10°W), a large nonlinear divergence is balanced by geostrophic and viscous divergence.

Overall, the weakness of the net divergence term confirms our interpretation of the vorticity Equation 16 as a diagnostic depth-integrated mass balance. In the interior of the subtropical and equatorial north Atlantic, we find the classical and expected balance between Ekman convergence (resp. divergence) and geostrophic divergence (resp. convergence). However, along western boundaries and at subpolar latitudes, the numerical torque is of leading-order. It corresponds to the artificial transport divergence that is felt by the flow because

of the inherent masking of u and v velocities in the C-grid discretization of the Coriolis force near boundaries (see Appendix B). This numerical torque is mostly balanced by geostrophic divergence, implying a mass adjustment to the spurious force. Text S6 in Supporting Information S1 confirms those results at the global scale.

5. Discussions

5.1. Comparison With Previous Work

Our ocean climate model analysis shows the relevance of wind-driven, topographic, viscous and numerical torques and the limited roles of bottom friction and nonlinear advection in vorticity balances of the depth-integrated flow. Here we discuss how those results compare to previous work. The dominance of the Sverdrup balance at subtropical latitudes is a classical result from ocean models at the large scale (Hughes & de Cuevas, 2001; Wang et al., 2017; Yeager, 2015). However, eddy-resolving simulations show that this balance breaks down locally as a result of nonlinear torques (Gula et al., 2015; Le Corre et al., 2020). In such models, it only emerges from horizontal integration over typically thousand kilometer scales. Topographic torques have also been well acknowledged along western boundaries and at subpolar latitudes (Ezer & Mellor, 1994; Hughes & de Cuevas, 2001; Le Bras et al., 2019; Le Corre et al., 2020; Myers et al., 1996; Schoonover et al., 2016; Spence et al., 2012; Styles et al., 2022; Wang et al., 2017; Yeager, 2015). In those regions, there is a consensus on their leading-order role in the depth-integrated, barotropic and geostrophic contour vorticity balances. Discretization issues related to the vorticity of the Coliolis force have only been documented by Bell (1999), Styles et al. (2022), to our knowledge. Only Styles et al. (2022) analyze in detail the origin and effects of those numerical torques in the BV equation. They identify, in agreement with our work, leading-order numerical torques in the vorticity balance of the subpolar Weddell Gyre circulation. We also note the presence of an often noisy diagnostic in numerous previous studies (e.g., Hughes & de Cuevas, 2001; Yeager, 2015), motivating in most cases some horizontal averaging procedure, and indicating probable numerical effects. Our model analysis also highlights large viscous effects. Previous work demonstrates that this is characteristic of non-eddying ocean simulations (Yeager, 2015) although it can also occur locally along western boundaries of eddy-rich simulations with geopotential vertical coordinates (Schoonover et al., 2016; Styles et al., 2022). As resolution increases, numerical viscosity is replaced by vigorous nonlinear advection in energetic areas such as western boundaries (Gula et al., 2015; Le Corre et al., 2020; Yeager, 2015). Conversely, in our global ocean climate configuration, nonlinear torques are weak and restricted to the deep Tropics. This result, classical at the non-eddying resolution, is in stark contrast with high-resolution runs where nonlinear advection becomes leading order everywhere energetic flows prevail (Gula et al., 2015; Le Corre et al., 2020; Wang et al., 2017; Yeager, 2015). Finally, intense bottom frictional torques are restricted to the western boundary of the Equatorial Atlantic. This is a common result among geopotential coordinate ocean models. Conversely, in terrain-following (e.g., sigma) coordinates, the absence of vertical side walls at the lateral boundaries, in better agreement with the mostly horizontal nature of ocean topography, leads to a dominant bottom stress curl along boundaries (Le Corre et al., 2020).

5.2. Addressing Numerical Torques

Among the main results from the vorticity balance discretization in the NEMO model is the presence of large numerical torques arising from the Coriolis force discretization in the C-grid. This issue has been thoroughly addressed for the BV equation by Styles et al. (2022) and we have extended the analysis to the alternatives vorticity equations for the depth-integrated flow. First, we discuss the configuration dependence, given a C-grid numerical platform with geopotential vertical coordinates. Numerical torques are a function of bottom and lateral boundary velocities. Therefore, they are circulation-dependent: the more baroclinic the flow, the weaker the numerical torques. This is evident when comparing numerical torques between the interior subtropical and subpolar regions of the north Atlantic (Figures 3–6). They are also bathymetry-dependent: the flatter the bathymetry, the less masking induced by double averaging in the C-grid, and therefore the weaker the spurious forces within the domain, as illustrated by the flat configuration of Styles et al. (2022). Finally, it is also resolution-dependent to the extent that resolution modifies both the circulation and bathymetry. With stronger boundary currents and rougher bathymetry, we expect at least as high numerical Coriolis torques at higher resolution, as confirmed by results from Styles et al. (2022) at the eddy-permitting resolution.

In their Section 6, Styles et al. (2022) discuss extensively possible numerical methods to mitigate these spurious forces. In particular, they discuss alternative Coriolis schemes, vorticity equations, finite difference grids (the B-grid) and vertical coordinates (sigma and isopycnal coordinates). They use the B-grid to demonstrate that changing the grid geometry can resolve the spurious Coriolis torques. We share their conclusions, and propose two extra ways forward. First, we have shown that the depth-integrated vorticity equation is an alternative to the BV equation which retains most of the depth-integrated flow while removing most of the spurious Coriolis torques (compare Figure 3 to Figure 4). Although it does not resolve any of the numerical issues identified here and in Styles et al. (2022), from a model analysis perspective, we strongly advise for a preferred use of this former equation. Second, we no not exclude the possibility for some alternative C-grid Coriolis discretization to remove such spurious torques. Namely, using a Coriolis scheme that conserves both the Coriolis parameter and the total mass transport would remove both the numerical beta effect and vortex stretching. It is not the case for the existing Coriolis schemes in C-grid ocean models.

6. Conclusions

Seminal theories on the oceanic gyre circulation are based on BV balances of the flow. In this work, we propose a theoretical framework for the analysis of momentum and vorticity balances of the ocean circulation. We show the existence of four distinct vorticity equations for the depth-integrated ocean circulation: the depth-integrated, barotropic, geostrophic contour and transport divergence vorticity balances. Each gives information, and provides extra constraints, on oceanic transports, through the involvement of horizontal velocities in the torque of the Coriolis force. The first two balances constrain the depth-integrated meridional transport, while the latter two describe transports across geostrophic contours and depth-integrated transport divergence, respectively. We stress the key role played by topographic torques in those balances, appearing as a bottom vortex stretching, a bottom pressure torque, a baroclinic pressure torque (the joint effect of baroclinicity and relief, JEBAR), or a geostrophic transport divergence, respectively. We propose depth-dependent counterparts for those equations where the interior vortex stretching is shown to play a key role as a coupling agent between vertical oceanic sublayers.

We then use the NEMO platform to address the complex issue of expressing the discretized form of those vorticity equations in ocean models. We show that the treatment of lateral boundaries and the Coriolis force discretization in C-grid ocean models are key to interpreting vorticity balances in ocean models, and we propose an interpretation for the discretized equations in the NEMO model. We show that discretization of the Coriolis parameter causes a spurious numerical beta effect near the topography, while the double averaging of velocities inherent to C-grid ocean models causes a spurious numerical planetary vortex stretching, again near the topography. We provide a comprehensive diagnostic toolbox aiming at computing such vorticity balances in C-grid ocean models, and specifically in the NEMO model.

Analysis of oceanic vorticity balances in a 500-year pre-industrial control run of the CNRM-CM6 climate model using a NEMO ocean component confirms that vorticity equations provide a wealth of dynamical constraints involving second-order terms of the momentum equations. In the model, three behaviors stand out: wind-driven balances, topographic constraints and numerical effects. In the depth-integrated and BV equations, the classical Sverdrup balance prevails in the interior of subtropical gyres. Topographic balances, driven by the bottom vortex stretching and bottom pressure torque, respectively, dominate over subpolar latitudes and along western boundaries. Bottom velocities as low as a few mm/s are sufficient for those torques to dominate the vorticity balance. Conversely, the geostrophic contour vorticity equation stresses the relevance of the flow baroclinicity, through JEBAR, which tends to suppress the topographic constraint. The dominance of this baroclinic torque highlights limitations of the topographic Sverdrup balance and of barotropic models of the oceanic circulation. Finally, the transport divergence vorticity equation confirms the balance between geostrophic and Ekman divergences over the interior of subtropical and tropical gyres. However, numerical torques arising from the discretization of the Coriolis force in C-grid models are significant in all vorticity balances derived from the depth-integrated momentum equation. They affect the flow which feels spurious divergences and variations of the Coriolis parameter and has to adjust its mass and circulation to balance them. Being topographic in essence, they are particularly large along western boundaries and at mid and high latitudes, where bottom velocities are significant. We suggest ways forward to address those numerical effects. Altogether, we believe that vorticity balances are helpful to interpret the barotropic circulation and improve ocean model numerics. Diagnosing them should become a more common practice in the ocean modeling community.

Appendix A: Complements on Oceanic Dynamical Balances

A1. Derivation of the Ocean's Boussinesq Momentum Equations

The large-scale ocean circulation is driven by the Boussinesq momentum equations which write in the local Cartesian coordinate frame as:

$$\frac{\partial \mathbf{u_h}}{\partial t} + (\mathbf{u}\cdot\boldsymbol{\nabla})\mathbf{u_h} + f\mathbf{k}\times\mathbf{u_h} = -\frac{1}{\rho_0}\boldsymbol{\nabla}P + \nu\Delta\mathbf{u_h} + b\mathbf{k} \tag{A1}$$

with $\mathbf{u_h}$ the horizontal velocity vector and $\mathbf{u}$ its three-dimensional counterpart, ∇ and Δ the Nabla and Laplacian operators, respectively, $f = 2\,\Omega\sin\phi$ the Coriolis parameter with Ω the Earth angular velocity and ϕ the latitude, $\mathbf{k}$ the local vertical unit vector, $\rho_0 = 1025$ kg/m^3 a reference seawater density, P the dynamical pressure, ν the kinematic viscosity of sea water and $b = -\frac{\rho}{\rho_0}g^*$ the buoyancy of sea water, with ρ the in situ density and $g^* = 9.81$ m/s^2 the local gravity acceleration including the planetary centrifugal forces. Equation A1 is written in the so-called advective form. It can equivalently be written in the so-called vector-invariant form by writing the nonlinear horizontal advection term as a purely rotational term plus a purely divergent term:

$$(\mathbf{u}_h.\boldsymbol{\nabla}_h)\mathbf{u_h} = \left[(\boldsymbol{\nabla}\times\mathbf{u})\times\mathbf{u} + \frac{1}{2}\nabla\mathbf{u}^2\right]_h \tag{A2}$$

where the right hand-side of Equation A2 is composed of the so-called relative vorticity advection and kinetic energy gradient terms.

Resolving ocean circulation requires a formal separation between the small-scale (unresolved) and the large-scale (resolved) components of motion. This is done by the classical Reynolds decomposition which yields, after averaging Equation A1 using Reynolds' axioms:

$$\frac{\partial \mathbf{u_h}}{\partial t} + (\mathbf{u}\cdot\boldsymbol{\nabla})\mathbf{u_h} + \boldsymbol{\nabla}\cdot\mathbf{R} + f\mathbf{k}\times\mathbf{u_h} = -\frac{1}{\rho_0}\boldsymbol{\nabla}P + b\mathbf{k} \tag{A3}$$

where for simplicity $\mathbf{u_h}$, $\mathbf{u}$, P, and b now stand for the Reynolds average velocities, dynamic pressure and buoyancy. The molecular dissipation term has been removed from dimensional analysis. $\mathbf{R}$ is the Reynolds stress tensor representing the forcing of the Reynolds average velocities by the perturbation velocities such that:

$$R_{ij} = \overline{u_i' u_j'} \tag{A4}$$

with the prime and overbar denoting a Reynolds average and perturbation. In a stratified fluid, turbulent fluxes are anisotropic between the horizontal and vertical directions so that Reynolds stresses are formally separated. In addition, a classical diffusive closure of turbulence yields:

$$\boldsymbol{\nabla}\cdot\mathbf{R} = -(\boldsymbol{\nabla}_h\cdot\kappa_h\boldsymbol{\nabla}_h)\mathbf{u_h} - \frac{\partial}{\partial z}\left(\kappa_z\frac{\partial \mathbf{u_h}}{\partial z}\right) \tag{A5}$$

with κ_h and κ_z the turbulent horizontal and vertical momentum diffusivities (or viscosities), respectively. Note that in the context of ocean modeling, there is no rigorous closure of the Reynolds averaged momentum Equation A3, as the turbulent horizontal viscosity is added solely for numerical stability purposes. More generally, there exists a diversity of turbulence closures for $\mathbf{R}$, some of which are not diffusive, but the remainder of this work is independent of the exact formulation for Reynolds stresses. Finally, with the turbulent closure assumptions of Equation A5, we get the Reynolds averaged Boussinesq momentum equations:

$$\frac{\partial \mathbf{u_h}}{\partial t} + (\mathbf{u}.\boldsymbol{\nabla})\mathbf{u_h} - (\boldsymbol{\nabla}_h.\kappa_h\boldsymbol{\nabla}_h)\mathbf{u_h} - \frac{\partial}{\partial z}\left(\kappa_z\frac{\partial \mathbf{u_h}}{\partial z}\right) + f\mathbf{k}\times\mathbf{u_h} = -\frac{1}{\rho_0}\boldsymbol{\nabla}P + b\mathbf{k} \tag{A6}$$

The terms are respectively the local momentum trend, nonlinear advection (the inertial force), turbulent lateral diffusion (lateral dissipation), turbulent vertical diffusion (vertical friction), Coriolis force, pressure force and buoyancy force. We write a simplified expression for the horizontal and vertical components as follows:

$$\frac{\partial \mathbf{u_h}}{\partial t} = \mathbf{A} + \mathbf{D} + \mathbf{F} - f\mathbf{k}\times\mathbf{u_h} - \frac{1}{\rho_0}\boldsymbol{\nabla}_\mathbf{h}P \tag{A7}$$

$$\frac{\partial P}{\partial z} = -\rho g^* \tag{A8}$$

with **A**, **D**, and **F** standing for nonlinear advection, horizontal dissipation and vertical friction, respectively.

A2. Alternative Formulation for the Vorticity Equation

The nonlinear advection term of Equation 3 can be developed as follows:

$$\begin{aligned} \mathrm{Curl}(\mathbf{A}) &= \mathbf{k}\cdot(\boldsymbol{\nabla}\times(\mathbf{u}\cdot\boldsymbol{\nabla})\mathbf{u_h}) \\ &= -\mathbf{u}\cdot\boldsymbol{\nabla}\zeta + \zeta\frac{\partial w}{\partial z} - \mathbf{k}\cdot\left(\boldsymbol{\nabla}_h w\times\frac{\partial \mathbf{u_h}}{\partial z}\right) \end{aligned} \tag{A9}$$

The right-hand side terms of Equation A9 are the relative vorticity advection, the relative vortex stretching and the vortex tilting terms (e.g., Vallis, 2006). The vorticity Equation 3 can then be recast as:

$$\frac{\partial \zeta}{\partial t} = -\mathbf{u}\cdot\boldsymbol{\nabla}\zeta + \mathrm{Curl}(\mathbf{D}) + \mathrm{Curl}(\mathbf{F}) - \beta v + (\zeta + f)\frac{\partial w}{\partial z} - \mathbf{k}\cdot\left(\boldsymbol{\nabla}_h w\times\frac{\partial \mathbf{u_h}}{\partial z}\right) \tag{A10}$$

Equation A10 is useful to diagnose the material evolution of relative vorticity and to analyze vorticity redistributions by the processes of vorticity stretching and tilting. However, from a practical standpoint, Equation 3 is trivially deduced from the storage at low-frequency (typically monthly) of the momentum trend diagnostics, together with horizontal velocities. On the contrary, the advective decomposition performed to obtain Equation A10 requires to either code online the decomposition of the advective vorticity trend, implying significant human and computational cost, or to store at high frequency (typically hourly to daily) the three-dimensional velocity fields in order to deduce the terms from offline computation, with very large storage requirements and associated numerical costs. Therefore, in this work, we limit our analysis of the depth-dependent vorticity balance to Equation 3.

A3. The Goldsbrough-Stommel Circulation

Dropping the surface vertical velocity w_s from Equation 4 removes the so-called Goldsbrough-Stommel circulation forced by surface freshwater fluxes, which was shown to reach at most 2 Sv (1 Sv = $10^6 \mathrm{m}^3/\mathrm{s}$) (Huang & Schmitt, 1993). Indeed, the ocean surface kinematic boundary condition yields a relation between surface vertical velocities and freshwater exchanges as:

$$\begin{aligned} &\frac{d}{dt}(\eta - z)_s = P + R - E \\ \Rightarrow\quad &w_s = E - P - R + \frac{d\eta}{dt} \end{aligned} \tag{A11}$$

with E, P, and R the evaporation, precipitation and runoff rates, in m/s.

A4. Characteristics of the Depth-Integrated Momentum Equation

The geostrophic terms of Equation 9 involve three gradient functions. Mathematically, as pointed out by Hughes and Killworth (1995), this partial derivative equation includes 12 types of closed characteristics along which two of those terms vanish and the third term can be integrated provided the remaining "forcings" are known. This property has limited applicability for ocean modeling because integrating a dynamical balance along a contour which does not follow the model grid generally leads to large errors (e.g., Ezer and Mellor, 1994; Myers et al., 1996). This is the case for almost all characteristics of Equation 9, which are contours of constant f, h, f/h, Ψ, P_b, or χ. The only characteristic along which Equation 9 is easily integrated in a numerical model is that of constant f (namely, a zonal integration of its zonal component). Integration over a closed contour of constant f is only possible at the latitudes of the Drake Passage and north of Greenland. This operation cancels out the Coriolis and baroclinic pressure terms to yield the zonally-integrated barotropic zonal momentum equation, also named the form stress equation:

$$\frac{\partial \widetilde{U}}{\partial t} = \widetilde{<A_x>} + \widetilde{<D_x>} + \frac{1}{\rho_0}\left(\widetilde{\tau_{xs}} - \widetilde{\tau_{xb}}\right) + \frac{1}{\rho_0}\widetilde{P_b\frac{\partial h}{\partial x}} \tag{A12}$$

where $\tilde{a} = \int_{x_R+}^{x_R-} a dx$ is the circumpolar integration operator with x_R and a an arbitrary longitude and scalar, respectively. The last term of Equation A12 is the bottom form stress intuited first by Munk and Palmén (1951). Over the latitudes of the Drake Passage, Equation A12 gives formidable insight into the momentum balance of the Antarctic Circumpolar Current (Olbers et al., 2004). However, its meridional domain of applicability is very limited. Therefore in this work, we focus on vorticity balances rather than contour-integrated momentum balances derived from Equation 9.

A5. Relation Between Integral and Depth-Dependent Vorticity Balances

Equation 4 is the only depth-integrated vorticity equation disposing of a natural depth-dependent counterpart, namely the depth-dependent vorticity Equation 3. Both equations possess the same physical terms and Equation 3 can be partially integrated vertically to diagnose the vorticity coupling of sublayers or the contribution of an individual layer to the total BV balance. Partial integration of Equation 3 also yields a diagnostic equation for meridional transports within a given depth range or for vertical velocities. To simplify the comparison, we re-write Equation 3 by making the bottom vortex stretching explicit:

$$\frac{\partial \zeta}{\partial t} = \mathrm{Curl}(\mathbf{A}) + \mathrm{Curl}(\mathbf{D}) + \mathrm{Curl}(\mathbf{F}) - \beta v + f\left(\frac{\partial w}{\partial z} + f\frac{w_b}{h}\right) - f\frac{w_b}{h} \tag{A13}$$

Again, as in Equation 4, we have neglected the surface vortex stretching forced by freshwater fluxes (Equation A11) and driving a weak Goldsbrough-Stommel circulation. The first vorticity stretching term of Equation A13 is purely redistributive over the vertical: by construct, its depth integral vanishes. This interior vortex stretching is the main agent transferring vorticity vertically from one layer to the next. It highlights again the key role of vertical velocities in setting the oceanic vorticity balance. The last term of Equation A13 is the bottom vortex stretching per unit depth. Indeed, bottom velocities stretch the full water column and in the absence of an a priori profile of vertical stretching, a reasonable assumption is that the bottom stretching applies uniformly to the full water column. It stresses the constraint posed by the bottom flow throughout the ocean depth.

Depth-dependent vorticity balances can also be formulated for Equations 10, 12, and 16, by integrating partially Equation 3 over a sub-layer before cross-differentiating (e.g., Yeager, 2015). Indeed, the partial integral analog of Equation 9 is:

$$\frac{\partial \hat{\mathbf{u}}_\mathbf{h}}{\partial t} = \hat{\mathbf{A}} + \hat{\mathbf{D}} + \frac{1}{\rho_0}\hat{\mathbf{F}} - f\mathbf{k}\cdot\nabla_h\hat{\mathbf{u}}_\mathbf{h} - \frac{1}{\rho_0}(\Delta z \nabla_h P_{bz1} + \nabla_h(\chi_{z1} - \chi_{z2})) \tag{A14}$$

with $\hat{a} = \int_{z1}^{z2} a dz$ the integral operator between depths $z1$ and $z2$, $\Delta z = \max(z1,-h) - \max(z2,-h)$ the layer thickness, $P_{bz1} = P\,(z = \max(z1,-h))$ the pressure at the bottom of the layer and $\chi_{zi} = g^* \int_{zi}^{0} \rho z dz$ the partial baroclinic potential energy above the depth zi (with $i = 1$ or 2). Equation A14 can be cross-differentiated after dividing by 1, h, or f to obtain the contribution of the layer between $z1$ and $z2$ to the depth integral vorticity balances 10, 12, and 16, respectively. However, the drawbacks of this approach are twofold: first, contrary to Equation 4, there is no continuous expression for those partial integral vorticity balances which must be formulated over a finite number of discrete sub-layers. Second, such partial integration leads to much more limited simplifications of the geostrophic terms in Equation A14 than in its full depth analog (Equation 9). Indeed, the vorticity of Equation A14 includes a top plus bottom vortex stretching because the depth-integrated horizontal transport can diverge. In addition, the bottom pressure force is not integrated over the full depth anymore so that the partial integral analog of Equation 12 includes an extra bottom pressure contribution. Therefore we have respectively two, three and two extra terms for the partial integral analogs of Equations 10, 12, and 16. Henceforth, we will restrict our interpretation of depth-dependent vorticity balances to Equation A13 in relation to Equation 4.

Appendix B: Discretizations in a C-Grid Ocean Model

B1. Time Discretizations

A schematic of the time stepping procedure is proposed Figure B1. In NEMO 3.6 (Madec, 2008), under the leapfrog time stepping and the time-splitted formulation for the three-dimensional versus barotropic dynamics, discretization of Equation A1 writes as:

$$\begin{aligned}\mathbf{utrd}_{tot} &= \mathbf{utrd}_{rvo} + \mathbf{utrd}_{keg} + \mathbf{utrd}_{zad} + \mathbf{utrd}_{pvo} + \mathbf{utrd}_{ldf} + \mathbf{utrd}_{pg} + \mathbf{utrd}_{zdf} + \mathbf{utrd}_{atf} + \mathbf{utrd}_{ts} \\ &= \mathbf{utrd}_{adv} + \mathbf{utrd}_{pvo} + \mathbf{utrd}_{ldf} + \mathbf{utrd}_{pg} + \mathbf{utrd}_{zdf} + \mathbf{utrd}_{atf} + \mathbf{utrd}_{ts}\end{aligned} \tag{B1}$$

where **utrd** stands for horizontal velocity trend contributions in m/s^2, with the suffix tot for the total trend, rvo and keg the relative vorticity (rotational) and kinetic energy gradient (divergent) decomposition of the horizontal nonlinear advective trend (see Equation A2), zad the vertical advective trend, pvo the planetary vorticity (Coriolis) trend, pg the pressure gradient trend, ldf the lateral diffusion (dissipation) trend, zdf the baroclinic vertical diffusion (friction) trend, atf the Asselin time filtering trend and ts the time splitted trend. In what follows, all terms of the advective trend are merged into one single term $\mathbf{utrd}_{adv}$, noting that over most of the model domain this term is second-order (see next section).

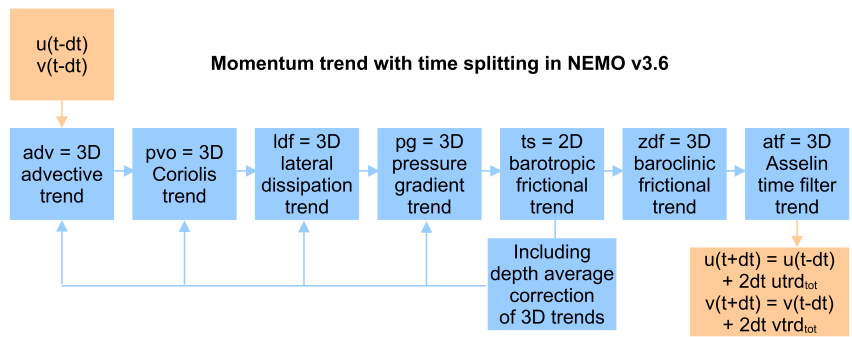

Figure B1. Time discretization of the horizontal momentum equation in NEMO 3.6 under time splitting of three-dimensional (baroclinic) and two-dimensional (barotropic) dynamics (Madec, 2008).

The two extra forces arising from the time discretization are the Asselin time filter (Leclair & Madec, 2009) that ensures convergence between odd and even time steps under the leapfrog discretization, and the time splitted trend arising from the separation between three-dimensional and barotropic dynamics (Madec, 2008). The former has been evaluated as a residual of Equation B1 and is negligible, as is the total trend which almost vanishes over the 500-year period (not shown). The latter includes the surface plus bottom friction trends, plus a small correction to the depth-average of the advective, viscous, Coriolis and pressure force trends which are also evaluated at the long baroclinic time step of the three-dimensional dynamics. However, in practice, this correction almost vanishes so that the time splitted trend merges surface plus bottom friction, that is the barotropic component of the vertical frictional trend. Hence, we deduce the bottom friction trend as the residual between the time splitted trend and the surface wind stress. Finally, we can write Equation B1 as:

$$0 \simeq \mathbf{utrd}_{adv} + \mathbf{utrd}_{pvo} + \mathbf{utrd}_{ldf} + \mathbf{utrd}_{pg} + \mathbf{utrd}_{zdf} \tag{B2}$$

where $\mathbf{utrd}_{zdf}$ now merges the total (baroclinic plus barotropic) vertical friction trend.

B2. Discretized Coriolis Force

In the NEMO model, the most widespread discretization of the Coriolis force is the so-called Energy and Enstrophy (EEN) conserving scheme (Madec, 2008). It has been shown to ensure conservation properties while at the same time reducing grid-scale noise in vertical velocity (Le Sommer et al., 2009) and producing a larger topostrophy of the flow (Penduff et al., 2007). This scheme formulates the zonal (resp. meridional) Coriolis force as a 4-point average of neighboring meridional (resp. zonal) velocities multiplied by so-called Coriolis triads. The key

to the stability and topostrophy of the scheme is the involvement of vertical scale factors in the computation of the model's Coriolis parameter and the masking of land points. Specifically, the u-grid and v-grid Coriolis parameters write under the EEN scheme at the location (i, j, k) as:

$$f_{u-EEN}(i,j,k) = \frac{e3u(i,j,k)}{3}\left(\frac{f_f(i,j,k)}{e3f(i,j,k)} + \frac{f_f(i-1,j,k)}{e3f(i-1,j,k)} + \frac{f_f(i,j-1,k)}{e3f(i,j-1,k)}\right) \tag{B3}$$

$$f_{v-EEN}(i,j,k) = \frac{e3v(i,j,k)}{3}\left(\frac{f_f(i,j,k)}{e3f(i,j,k)} + \frac{f_f(i-1,j,k)}{e3f(i-1,j,k)} + \frac{f_f(i,j-1,k)}{e3f(i,j-1,k)}\right) \tag{B4}$$

with e3f the f-grid vertical scale factor, and f_f the Coriolis parameter evaluated on the f-grid (see Figure 2). Note that over land points (where $e3f = 0$), the ratio $f_f/e3f$ is replaced by zero. As a result, f_{u-EEN} and f_{v-EEN} are systematically reduced near topography, which explains the larger topostrophy of the flow. Finally we obtain the zonal and meridional Coriolis trends as:

$$\begin{aligned} utrd_{pvo}(i,j,k) = \frac{umask(i,j,k)}{4\,e1u(i,j)}&([v\,e1v\,f_{v-EEN}](i,j,k) + [v\,e1v\,f_{v-EEN}](i+1,j,k) \\ &+[v\,e1v\,f_{v-EEN}](i,j-1,k) + [v\,e1v\,f_{v-EEN}](i+1,j-1,k)) \end{aligned} \tag{B5}$$

$$\begin{aligned} vtrd_{pvo}(i,j,k) = -\frac{vmask(i,j,k)}{4\,e2v(i,j)}&([u\,e2u\,f_{u-EEN}](i,j,k) + [u\,e2u\,f_{u-EEN}](i-1,j,k) \\ &+[u\,e2u\,f_{u-EEN}](i,j+1,k) + [u\,e2u\,f_{u-EEN}](i-1,j+1,k)) \end{aligned} \tag{B6}$$

with e1u and e1v the grid i-axis scale factor on u and v-points, e2u and e2v the grid j-axis scale factor on u and v-points, umask and vmask the three-dimensional land-sea masks over the u and v-grid (see Figure 2). The above equations are essentially a 4-point averaging of horizontal velocities taking into account the deformation of the curvilinear grid and with a modified Coriolis parameter.

We can now express the physical Coriolis trend by simply performing a 4-point average of horizontal transports in each direction times the actual Coriolis parameter:

$$\begin{aligned} utrd_{pvo-\mathrm{phys}}(i,j,k) = \frac{1}{4\,e1u(i,j)}&([v\,e1v\,f_v](i,j,k) + [v\,e1v\,f_v](i+1,j,k) \\ &+[v\,e1v\,f_v](i,j-1,k) + [v\,e1v\,f_v](i+1,j-1,k)) \end{aligned} \tag{B7}$$

$$\begin{aligned} vtrd_{pvo-\mathrm{phys}}(i,j,k) = -\frac{1}{4\,e2v(i,j)}&([u\,e2u\,f_u](i,j,k) + [u\,e2u\,f_u](i-1,j,k) \\ &+[u\,e2u\,f_u](i,j+1,k) + [u\,e2u\,f_u](i-1,j+1,k)) \end{aligned} \tag{B8}$$

We deduce the numerical Coriolis trend as the difference $B5 - B7$. It arises from the modification of the Coriolis parameter by the f triads of the EEN scheme. We also note that the masking performed in Equation B5 removes a fraction of horizontal transports located next to boundaries. We will see below that these numerical effects have large consequences on the model's vorticity equations.

B3. Discretized Coriolis Vorticity

From Equation 18, the vorticity of the total Coriolis trend writes as:

$$\begin{aligned} ztrd_{pvo} &= \mathrm{Curl}(\mathbf{utrd}_{pvo}) \\ &= \frac{1}{e1f\,e2f}\left(\delta_{i+1/2}(e2v\,vtrd_{pvo}) - \delta_{j+1/2}(e1u\,utrd_{pvo})\right) \\ &= -\frac{1}{4\,e1f\,e2f}\left(\delta_{i+1/2}\left(vmask\sum_{m=1}^{4}(u\,e2u\,f_{u-EEN})_m\right) + \delta_{j+1/2}\left(umask\sum_{m=1}^{4}(v\,e1v\,f_{v-EEN})_m\right)\right) \end{aligned} \tag{B9}$$

where for simplicity we have used an arbitrary m index for the 4-point averaging of equation B5. We can decompose it into a total beta effet plus a vortex stretching as:

$$\begin{aligned} ztrd_{pvo} = &-\frac{1}{4\,e1f\,e2f}\left(\sum_{m=1}^{4}\left(u\,e2u\,\delta_{i+1/2}(vmask\,f_{u-EEN})\right)_m + \sum_{m=1}^{4}\left(v\,e1v\,\delta_{j+1/2}(umask\,f_{v-EEN})\right)_m\right. \\ &\left. + \sum_{m=1}^{4}\left(f_{u-EEN}\,\delta_{i+1/2}(vmask\,u\,e2u)\right)_m + \sum_{m=1}^{4}\left(f_{v-EEN}\,\delta_{j+1/2}(umask\,v\,e1v)\right)_m\right) \\ = &\; ztrd_{beta} + ztrd_{stretch} \end{aligned} \tag{B10}$$

where the suffixes *beta* and stretch stand for the total planetary beta effect and vortex stretching, respectively. From Equation B10, we identify two numerical torques: as mentioned above, the Coriolis parameter is modified by the EEN scheme, which produces a numerical beta effect; in addition, the horizontal transport divergence lacks any vertical scale factor, which causes a numerical vortex stretching where those vertical scale factors vary spatially. Note that because of the 4-point averaging of velocities, reformulating the curl operator of Equation 18 with vertical scale factors does not remove this numerical effect, which is inherent to the C-grid. Both effects cancel out where vertical scale factors are homogeneous, that is away from topography. Therefore, they can be interpreted as numerical topographic torques.

To decompose the physical and numerical beta effect and vortex stretching, we write the physical contributions:

$$ztrd_{beta-\mathrm{phys}} = -\frac{1}{4\,e1f\,e2f}\left(\sum_{m=1}^{4}\left(u\,e2u\,\delta_{i+1/2}f_u\right)_m + \sum_{m=1}^{4}\left(v\,e1v\,\delta_{j+1/2}f_v\right)_m\right) \tag{B11}$$

$$ztrd_{stretch-\mathrm{phys}} = -\frac{1}{4\,e1f\,e2f\,e3f}\left(\sum_{m=1}^{4}\left(f_u\,\delta_{i+1/2}(u\,e2u\,e3u)\right)_m + \sum_{m=1}^{4}\left(f_v\,\delta_{j+1/2}(v\,e1v\,e3v)\right)_m\right) \tag{B12}$$

where the suffixes $beta-phys$ and $stretch-phys$ stand for the physical planetary beta effect and vortex stretching, respectively. The physical beta effect is the 4-point averaged variation of the actual Coriolis parameter times velocities. The physical vortex stretching is the 4-point averaged horizontal transport divergence per unit depth (including vertical scale factors) times the physical Coriolis parameter. Note that as no masked point is considered in the vorticity trend computation, the removal of masks in Equation B11 has no consequence. Finally, we deduce numerical Coriolis torques as the difference $B10 - B11$.

B4. Discretized Vorticity of the Depth-Integrated Coriolis Force

We now consider the Coriolis torques derived from the depth-integrated momentum Equation 9 (see Figure 2 for an illustration). Depth-integration prior to cross-differentiating causes two extra difficulties in the separation between physical and numerical torques: some crossed numerical effects arise from vertical integration; and the masking of velocities inherent to interpolations from the u-grid to the v-grid (and conversely) under the Arakawa-C grid causes a large numerical torque. Indeed, following Equation 19, the torque of the depth-integrated Coriolis force writes as:

$$\begin{aligned} Ztrd_{pvo} &= \mathrm{Curl}\left(\int_{-h}^{0}\mathbf{utrd}_{pvo}dz\right) \\ &= \frac{1}{e1f\,e2f}\left(\delta_{i+1/2}\left(e2v\sum_k vtrd_{pvo}e3v\right) - \delta_{j+1/2}\left(e1u\sum_k utrd_{pvo}e3u\right)\right) \\ &= -\frac{1}{e1f\,e2f}\left(\delta_{i+1/2}vmask\sum_k e3v\sum_{m=1}^{4}\frac{(e2u\,u\,f_{u-EEN})_m}{4} + \delta_{j+1/2}umask\sum_k e3u\sum_{m=1}^{4}\frac{(e1v\,v\,f_{v-EEN})_m}{4}\right) \end{aligned} \tag{B13}$$

We identify again a numerical beta effect caused by modifications of the Coriolis parameter due to the EEN scheme. In addition, the depth-integrated horizontal transport divergence, which should be near zero (by mass conservation), is affected by the masking of velocities inherent to the interpolation from the u-grid to the v-grid (and reversely), which removes a fraction of the transport next to land points. This results again in a numerical vortex stretching, which is this time intrinsic to the Coriolis force formulation in the C-grid.

Decomposition of Equation B13 into a total beta effect and vortex stretching yields a numerical crossed term due to the depth-dependent Coriolis parameter in the EEN scheme. Indeed, we have:

$$Ztrd_{beta} = -\frac{1}{e1f\ e2f}\left(\frac{\sum_k e3v\ \sum_{m=1}^{4}(e2u\,u)_m}{4\sum_k e3v}\delta_{i+1/2}\,vmask\sum_k e3v\sum_{m=1}^{4}\frac{(f_{u-EEN})_m}{4} + \frac{\sum_k e3u\ \sum_{m=1}^{4}(e1v\,v)_m}{4\sum_k e3u}\delta_{i+1/2}\,umask\sum_k e3u\sum_{m=1}^{4}\frac{(f_{v-EEN})_m}{4}\right) \tag{B14}$$

$$Ztrd_{stretch} = -\frac{1}{e1f\ e2f}\left(\frac{\sum_k e3v\ \sum_{m=1}^{4}(f_{u-EEN})_m}{4\sum_k e3v}\delta_{i+1/2}\,vmask\sum_k e3v\sum_{m=1}^{4}\frac{(e2u\,u)_m}{4} + \frac{\sum_k e3u\ \sum_{m=1}^{4}(f_{v-EEN})_m}{4\sum_k e3u}\delta_{i+1/2}\,umask\sum_k e3u\sum_{m=1}^{4}\frac{(e1v\,v)_m}{4}\right) \tag{B15}$$

$$Ztrd_{cross} = Ztrd_{pvo} - Ztrd_{beta} - Ztrd_{stretch} \tag{B16}$$

where the suffixes *beta*, stretch, and *cross* stand for the total planetary beta effect, vortex stretching and the crossed numerical torque, respectively. We have multiplied the depth average transport by the depth integral Coriolis variations to get the beta effect, and conversely for the vortex stretching.

Finally, we can again decompose the beta effect and stretching terms into a physical and numerical contribution by expressing physical torques as:

$$Ztrd_{beta-\mathrm{phys}} = -\frac{1}{e1f\ e2f}\left(\left(\sum_k e3v\sum_{m=1}^{4}(e2u\,u)_m\right)\delta_{i+1/2}\sum_{m=1}^{4}\frac{(f_u)_m}{4} + \left(\sum_k e3u\sum_{m=1}^{4}(e1v\,v)_m\right)\delta_{i+1/2}\sum_{m=1}^{4}\frac{(f_v)_m}{4}\right) \tag{B17}$$

$$Ztrd_{stretch-\mathrm{phys}} = -\frac{1}{e1f\ e2f}\left(\sum_{m=1}^{4}(f_u)_m\delta_{i+1/2}\sum_k\sum_{m=1}^{4}\frac{(e2u\,e3u\,u)_m}{4} + \sum_{m=1}^{4}(f_v)_m\delta_{i+1/2}\sum_k\sum_{m=1}^{4}\frac{(e1v\,e3v\,v)_m}{4}\right) \tag{B18}$$

The physical Coriolis parameter is depth-independent, so that no crossed torque arises from depth integration. As for the physical stretching term, it is the discretized form of the Goldsbrough-Stommel effect, which is second-order. The main difference between the physical and total stretching is the masking of horizontal velocities in the latter case, which yields a large artificial depth-integrated divergence. We can finally deduce numerical Coriolis torques as the difference $B14 - B17$. We end up with five Coriolis torques, two physical (including one second-order effect) and three numerical.

We now consider the two alternative vorticity equations derived from the depth-integrated momentum Equation 9 (Equations 12 and 16). The situation is identical to the BV equation: three extra numerical torques arise from the Coriolis force discretization. In the vorticity equation for the depth-averaged momentum balance, the numerical beta effect is an artificial transport across geostrophic contours caused by the numerical modification of f. The numerical stretching is driven by a transport divergence per unit depth caused by the masking of velocity points by the averaging procedure inherent to the C-grid. Again, the physical component of this term is the Goldsbrough-Stommel effect and largely second-order. Finally, as the model geostrophic contours are depth-dependent, a crossed numerical torque arises from the vertical covariance of transports and f_{EEN}. We end up again with five Coriolis torques, two physical (including one second-order effect) and three numerical.

Regarding the transport vorticity equation, the beta effect should be identically zero because the Coriolis force has been divided by f prior to cross-differentiation. However, because of the model discretization, a numerical torque arises from the deviation of f from its physical value, which in turn drives a transport divergence. The stretching term, whose physical component is the depth-integrated transport divergence and should be near zero, has an extra numerical torque related to the masking of velocities. This again drives a torque that causes transport divergence. Finally, a crossed numerical torque arises from vertical integration. This time, we end up with four Coriolis torques, one second-order physical effect and three numerical ones.

Data Availability Statement

All the data and source code that have served for this analysis can be found in github.com, within the project RobinWaldman/VoBiN. The model grid and output files used for the analysis can be downloaded on zenodo under the https://doi.org/10.5281/zenodo.7788411. The NEMO v3.6 code can be publicly accessed via: www.nemo-ocean.eu.

Acknowledgments
This work was funded by the European Union's Horizon 2020 research and innovation programme under grant agreement No. 101003536 (ESM2025–Earth System Models for the Future). We kindly thank Stephen Griffies for useful advice, Andrew Styles for fruitful discussions and code sharing, and two anonymous reviewers.

References

Arakawa, A., & Lamb, V. R. (1977). Computational design of the basic dynamical processes of the UCLA general. *Circulation Model*, 173–265. https://doi.org/10.1016/b978-0-12-460817-7.50009-4

Bell, M. J. (1999). Vortex stretching and bottom torques in the Bryan-Cox ocean circulation model. *Journal of Geophysical Research*, *104*(C10), 23545–23563. https://doi.org/10.1029/1999jc900064

Blanke, B., & Delecluse, P. (1993). Variability of the tropical {A}tlantic ocean simulated by a general circulation model with two different mixed layer physics. *Journal of Physical Oceanography*, *23*(7), 1363–1388. https://doi.org/10.1175/1520-0485(1993)023<1363:vottao>2.0.co;2

Böning, C. W. (1986). On the influence of frictional parameterization in wind-driven ocean circulation models. *Dynamics of Atmospheres and Oceans*, *10*(1), 63–92. https://doi.org/10.1016/0377-0265(86)90010-2

Böning, C. W., Dispert, A., Visbeck, M., Rintoul, S. R., & Schwarzkopf, F. U. (2008). The response of the Antarctic Circumpolar Current to recent climate change. *Nature Geoscience*, *1*(12), 864–869. https://doi.org/10.1038/ngeo362

Borowski, D., Gerdes, R., & Olbers, D. (2002). Thermohaline and wind forcing of a circumpolar channel with blocked geostrophic contours. *Journal of Physical Oceanography*, *32*(9), 2520–2540. https://doi.org/10.1175/1520-0485(2002)032¡2520:TAWFOA¿2.0.CO;2

Bryan, K., & Cox, M. D. (1972). The circulation of the world ocean: A numerical study. Part I, A homogeneous model. *Journal of Physical Oceanography*, *2*(4), 319–335. https://doi.org/10.1175/1520-0485(1972)002¡0319:TCOTWO¿2.0.CO;2

Chevallier, M., y Mélia, D., Voldoire, A., Déqué, M., & Garric, G. (2013). Seasonal forecasts of the pan-arctic sea ice extent using a GCM-based seasonal prediction system. *Journal of Climate*, *26*(16), 6092–6104. https://doi.org/10.1175/JCLI-D-12-00612.1

Craig, A., Valcke, S., & Coquart, L. (2017). Development and performance of a new version of the OASIS coupler, OASIS3-MCT_3.0. *Geoscientific Model Development*, *10*(9), 3297–3308. https://doi.org/10.5194/gmd-10-3297-2017

Decharme, B., Delire, C., Minvielle, M., Colin, J., Vergnes, J.-P., Alias, A., et al. (2019). Recent Changes in the ISBA-CTRIP land surface system for use in the CNRM-CM6 climate model and in global off-line hydrological applications. *Journal of Advances in Modeling Earth Systems*, *11*(5), 1207–1252. https://doi.org/10.1029/2018MS001545

de Lavergne, C., Falahat, S., Madec, G., Roquet, F., Nycander, J., & Vic, C. (2019). Toward global maps of internal tide energy sinks. *Ocean Modelling*, *137*, 52–75. https://doi.org/10.1016/j.ocemod.2019.03.010

de Lavergne, C., Madec, G., Le Sommer, J., Nurser, A. J. G., & Naveira Garabato, A. C. (2016). The impact of a variable mixing efficiency on the abyssal overturning. *Journal of Physical Oceanography*, *46*(2), 663–681. https://doi.org/10.1175/JPO-D-14-0259.1

Eyring, V., Bony, S., Meehl, G. A., Senior, C. A., Stevens, B., Stouffer, R. J., & Taylor, K. E. (2016). Overview of the Coupled Model Intercomparison Project Phase 6 (CMIP6) experimental design and organization. *Geoscientific Model Development*, *9*(5), 1937–1958. https://doi.org/10.5194/gmd-9-1937-2016

Ezer, T., & Mellor, G. L. (1994). Diagnostic and prognostic calculations of the North Atlantic circulation and sea level using a sigma coordinate ocean model. *Journal of Geophysical Research*, *99*(C7), 14159. https://doi.org/10.1029/94jc00859

Fairall, C. W., Bradley, E. F., Hare, J. E., Grachev, A. A., & Edson, J. B. (2003). Bulk parameterization of air-sea fluxes: Updates and verification for the COARE algorithm. *Journal of Climate*, *16*(4), 571–591. https://doi.org/10.1175/1520-0442(2003)016<0571:bpoasf>2.0.co;2

Fofonoff, N. P. (1954). Steady flow in a frictionless homogeneous ocean. *Journal of Marine Research*, *13*, 254–262.

Fox-Kemper, B., Ferrari, R., & Hallberg, R. (2008). Parameterization of mixed layer eddies. Part I: Theory and Diagnosis. *Journal of Physical Oceanography*, *38*(6), 1145–1165. https://doi.org/10.1175/2007JPO3792.1

Ganachaud, A., & Wunsch, C. (2000). Improved estimates of global ocean circulation, heat transport and mixing from hydrographic data. *Nature*, *408*(6811), 453–457. https://doi.org/10.1038/35044048

Gula, J., Molemaker, M. J., & McWilliams, J. C. (2015). Gulf Stream dynamics along the southeastern U.S. seaboard. *Journal of Physical Oceanography*, *45*(3), 690–715. https://doi.org/10.1175/JPO-D-14-0154.1

Hendershott, M. C., & Rizzoli, P. (1976). The winter circulation of the Adriatic Sea. *Deep-Sea Research and Oceanographic Abstracts*, *23*(5), 353–370. https://doi.org/10.1016/0011-7471(76)90834-2

Holland, W. R. (1973). Baroclinic and topographic influences on the transport in western boundary currents. *Geophysical Fluid Dynamics*, *4*(3), 187–210. https://doi.org/10.1080/03091927208236095

Huang, R. X., & Schmitt, R. W. (1993). The Goldsbrough-Stommel circulation of the world oceans. *Journal of Physical Oceanography*, *23*(6), 1277–1284. https://doi.org/10.1175/1520-0485(1993)023¡1277:TGCOTW¿2.0.CO;2

Hughes, C. W., & de Cuevas, B. A. (2001). Why western boundary currents in realistic oceans are inviscid: A link between form stress and bottom pressure torques. *Journal of Physical Oceanography*, *31*(10), 2871–2885. https://doi.org/10.1175/1520-0485(2001)031¡2871:WWBCIR¿2.0.CO;2

Hughes, C. W., & Killworth, P. D. (1995). Effects of bottom topography in the large-scale circulation of the Southern Ocean. *Journal of Physical Oceanography*, *25*(11), 2485–2497. https://doi.org/10.1175/1520-0485(1995)025¡2485:EOBTIT¿2.0.CO;2

Jackson, L., Hughes, C. W., & Williams, R. G. (2006). Topographic control of basin and channel flows: The role of bottom pressure torques and friction. *Journal of Physical Oceanography*, *36*(9), 1786–1805. https://doi.org/10.1175/JPO2936.1

Jagannathan, A., Srinivasan, K., McWilliams, J. C., Jeroen Molemaker, M., & Stewart, A. L. (2021). Boundary-layer-mediated vorticity generation in currents over sloping bathymetry. *Journal of Physical Oceanography*. https://doi.org/10.1175/JPO-D-20-0253.1

Jouanno, J., & Capet, X. (2020). Connecting flow-topography interactions, vorticity balance, baroclinic instability and transport in the Southern Ocean: The case of an idealized storm track. *Ocean Science*, *16*(5), 1207–1223. https://doi.org/10.5194/os-16-1207-2020

LaCasce, J. H., & Isachsen, P. E. (2010). The linear models of the ACC. *Progress in Oceanography*, *84*(3), 139–157. https://doi.org/10.1016/j.pocean.2009.11.002

Le Bras, I. A. A., Sonnewald, M., & Toole, J. M. (2019). A barotropic vorticity budget for the subtropical north Atlantic based on observations. *Journal of Physical Oceanography*, *49*(11), 2781–2797. https://doi.org/10.1175/JPO-D-19-0111.1

Leclair, M., & Madec, G. (2009). A conservative leapfrog time stepping method. *Ocean Modelling*, *30*(2–3), 88–94. https://doi.org/10.1016/j.ocemod.2009.06.006

Le Corre, M., Gula, J., & Tréguier, A. M. (2020). Barotropic vorticity balance of the North Atlantic subpolar gyre in an eddy-resolving model. *Ocean Science*, *16*(2), 451–468. https://doi.org/10.5194/os-16-451-2020

Le Sommer, J., Penduff, T., Theetten, S., Madec, G., & Barnier, B. (2009). How momentum advection schemes influence current-topography interactions at eddy permitting resolution. *Ocean Modelling*, *29*(1), 1–14. https://doi.org/10.1016/j.ocemod.2008.11.007

Madec, G. (2008). Nemo ocean engine.

Mertz, G., & Wright, D. G. (1992). Interpretations of the JEBAR term. *Journal of Physical Oceanography*, *22*(3), 301–305. https://doi.org/10.1175/1520-0485(1992)022¡0301:iotjt¿2.0.co;2

Mesinger, F., & Arakawa, A. (1976). Numerical methods used in atmospheric models, volume 1. In *Global atmospheric research program world meteorological organization* (Vol. 1).

Munk, W. H. (1950). On the wind-driven ocean circulation. *Journal of the Atmospheric Sciences*, *7*(2), 80–93. https://doi.org/10.1175/1520-0469(1950)007¡0080:OTWDOC¿2.0.CO;2

Munk, W. H., & Palmén, E. (1951). Note on the dynamics of the Antarctic circumpolar current. *Tellus*, *3*(1), 53–55. https://doi.org/10.3402/tellusa.v3i1.8609

Myers, P. G., Fanning, A. F., & Weaver, A. J. (1996). JEBAR, bottom pressure torque, and Gulf Stream separation. *Journal of Physical Oceanography*, *26*(5), 671–683. https://doi.org/10.1175/1520-0485(1996)026¡0671:JBPTAG¿2.0.CO;2

Olbers, D., Borowski, D., Völker, C., & Wölff, J.-O. (2004). The dynamical balance, transport and circulation of the Antarctic circumpolar current. *Antarctic Science*, *16*(4), 439–470. https://doi.org/10.1017/S0954102004002251

Olbers, D., & Eden, C. (2003). A simplified general circulation model for a baroclinic ocean with topography. Part I: Theory, waves, and wind-driven circulations. *Journal of Physical Oceanography*, *33*(12), 2719–2737. https://doi.org/10.1175/1520-0485(2003)033¡2719:ASGCMF¿2.0.CO;2

Olbers, D., & Lettmann, K. (2007). Barotropic and baroclinic processes in the transport variability of the Antarctic Circumpolar Current. *Ocean Dynamics*, *57*(6), 559–578. https://doi.org/10.1007/s10236-007-0126-1

Patmore, R. D., Holland, P. R., Munday, D. R., Garabato, A. C. N., Stevens, D. P., & Meredith, M. P. (2019). Topographic control of Southern Ocean gyres and the Antarctic circumpolar current: A barotropic perspective. *Journal of Physical Oceanography*, *49*(12), 3221–3244. https://doi.org/10.1175/JPO-D-19-0083.1

Pedlosky, J. (1996). Ocean circulation theory. *Ocean Circulation Theory*. https://doi.org/10.1007/978-3-662-03204-6

Penduff, T., Le Sommer, J., Barnier, B., Treguier, A. M., Molines, J. M., & Madec, G. (2007). Influence of numerical schemes on current-topography interactions in 1/4° global ocean simulations. *Ocean Science*, *3*(4), 509–524. https://doi.org/10.5194/os-3-509-2007

Redi, M. H. (1982). Oceanic isopycnal mixing by coordinate rotation. *Journal of Physical Oceanography*, *12*(10), 1154–1158. https://doi.org/10.1175/1520-0485(1982)012¡1154:OIMBCR¿2.0.CO;2

Renault, L., McWilliams, J. C., & Penven, P. (2017). Modulation of the Agulhas Current retroflection and leakage by oceanic current interaction with the atmosphere in coupled simulations. *Journal of Physical Oceanography*, *47*(8), 2077–2100. https://doi.org/10.1175/JPO-D-16-0168.1

Rhines, P. B. (1986). Vorticity dynamics of the oceanic general circulation. *Annual Review of Fluid Mechanics*, *18*(1), 433–497. https://doi.org/10.1146/annurev.fl.18.010186.002245

Saenko, O. A., Fyfe, J. C., & England, M. H. (2005). On the response of the oceanic wind-driven circulation to atmospheric CO_2 increase. *Climate Dynamics*, *25*(4), 415–426. https://doi.org/10.1007/s00382-005-0032-5

Sarkisyan, A. S., & Ivanov, F. F. (1971). Joint effect of baroclinicity and bottom relief as an important factor in the dynamics of the sea currents. *Investiya Academy of Sciences, USSR, Atmospheric and Ocean Sciences*, *1*, 173–188.

Schoonover, J., Dewar, W., Wienders, N., Gula, J., McWilliams, J. C., Molemaker, M. J., et al. (2016). North Atlantic barotropic vorticity balances in numerical models. *Journal of Physical Oceanography*, *46*(1), 289–303. https://doi.org/10.1175/JPO-D-15-0133.1

Sonnewald, M., Wunsch, C., & Heimbach, P. (2019). Unsupervised learning reveals geography of global ocean dynamical regions. *Earth and Space Science*, *6*(5), 784–794. https://doi.org/10.1029/2018EA000519

Spence, P., Saenko, O. A., Sijp, W., & England, M. (2012). The role of bottom pressure torques on the interior pathways of north Atlantic deep water. *Journal of Physical Oceanography*, *42*(1), 110–125. https://doi.org/10.1175/2011JPO4584.1

Stewart, A. L., McWilliams, J. C., & Solodoch, A. (2021). On the role of bottom pressure torques in wind-driven gyres. *Journal of Physical Oceanography*, *51*(5), 1441–1464. https://doi.org/10.1175/JPO-D-20-0147.1

Stommel, H. (1948). The westward intensification of wind-driven ocean currents. *Eos, Transactions American Geophysical Union*, *29*(2), 202–206. https://doi.org/10.1029/TR029i002p00202

Styles, A. F., Bell, M. J., Marshall, D. P., & Storkey, D. (2022). Spurious forces can dominate the vorticity budget of ocean gyres on the c-grid. *Journal of Advances in Modeling Earth Systems*, *14*(5), e2021MS002. https://doi.org/10.1029/2021MS002884

Sverdrup, H. U. (1947). Wind-driven currents in a baroclinic ocean; with application to the equatorial currents of the eastern Pacific. *Proceedings of the National Academy of Sciences*, *33*(11), 318–326. https://doi.org/10.1073/pnas.33.11.318

Thomas, M. D., Boer, A. M. D., Johnson, H. L., & Stevens, D. P. (2014). Spatial and temporal scales of Sverdrup balance. *Journal of Physical Oceanography*, *44*(10), 2644–2660. https://doi.org/10.1175/JPO-D-13-0192.1

Vallis, G. K. (2006). *Atmospheric and oceanic fluid dynamics* (p. 745). Cambridge University Press.

Visbeck, M., Marshall, J., Haine, T., & Spall, M. (1997). Specification of eddy transfer coefficients in coarse-resolution ocean circulation models. *Journal of Physical Oceanography*, *27*(3), 381–402. https://doi.org/10.1175/1520-0485(1997)027¡0381:SOETCI¿2.0.CO;2

Voldoire, A., Saint-Martin, D., Sénési, S., Decharme, B., Alias, A., Chevallier, M., et al. (2019). Evaluation of CMIP6 DECK experiments with CNRM-CM6-1. *Journal of Advances in Modeling Earth Systems*, *11*(7), 2177–2213. https://doi.org/10.1029/2019MS001683

Voldoire, A., Sanchez-Gomez, E., y Mélia, D., Decharme, B., Cassou, C., Sénési, S., et al. (2013). The CNRM-CM5.1 global climate model: Description and basic evaluation. *Climate Dynamics*, *40*(9), 2091–2121. https://doi.org/10.1007/s00382-011-1259-y

Waldman, R., Hirschi, J., Voldoire, A., Cassou, C., & Msadek, R. (2020). Clarifying the relation between AMOC and thermal wind: Application to the centennial variability in a coupled climate model. *Journal of Physical Oceanography*, *51*(2), 343–364. https://doi.org/10.1175/jpo-d-19-0284.1

Wang, Y., Claus, M., Greatbatch, R. J., & Sheng, J. (2017). Decomposition of the mean barotropic transport in a high-resolution model of the North Atlantic Ocean. *Geophysical Research Letters*, *44*(22), 11537–11546. https://doi.org/10.1002/2017GL074825

Yeager, S. (2015). Topographic coupling of the Atlantic overturning and gyre circulations. *Journal of Physical Oceanography*, *45*(5), 1258–1284. https://doi.org/10.1175/JPO-D-14-0100.1